NACA RM L56I07

NACA

RESEARCH MEMORANDUM

EXPERIMENTAL INVESTIGATION OF THE AERODYNAMIC LOADING ON A HELICOPTER ROTOR BLADE IN FORWARD FLIGHT

By John P. Rabbott, Jr., and Gary B. Churchill

Langley Aeronautical Laboratory
Langley Field, Va.

NATIONAL ADVISORY COMMITTEE
FOR AERONAUTICS

WASHINGTON

October 25, 1956
Declassified October 14, 1957

ERRATA NO. 2

NACA Research Memorandum L56I07

By John P. Rabbott, Jr., and Gary B. Churchill
October 1956

Page 26: Replace figure 4 with corrected figure 4 attached. The error corrected is in the curve labeled b_1 in the lower plot (fig. 4(b)).

Issued 12-6-57

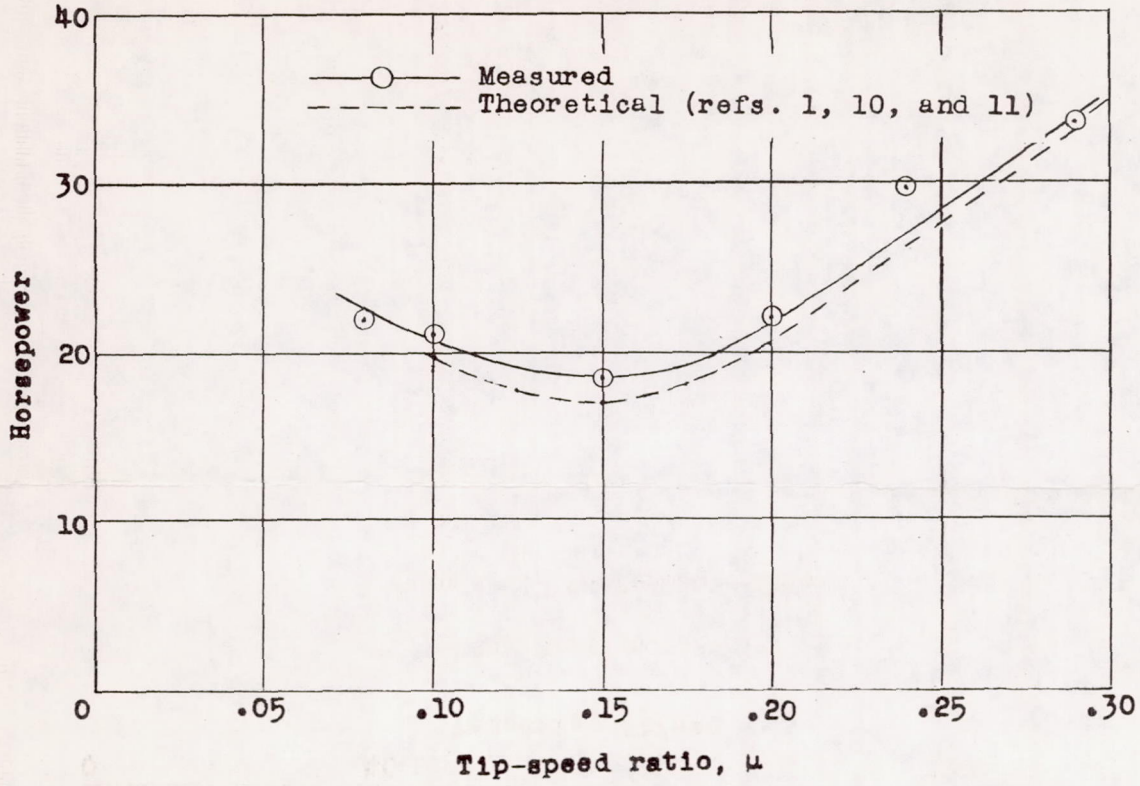

(a) Power required.

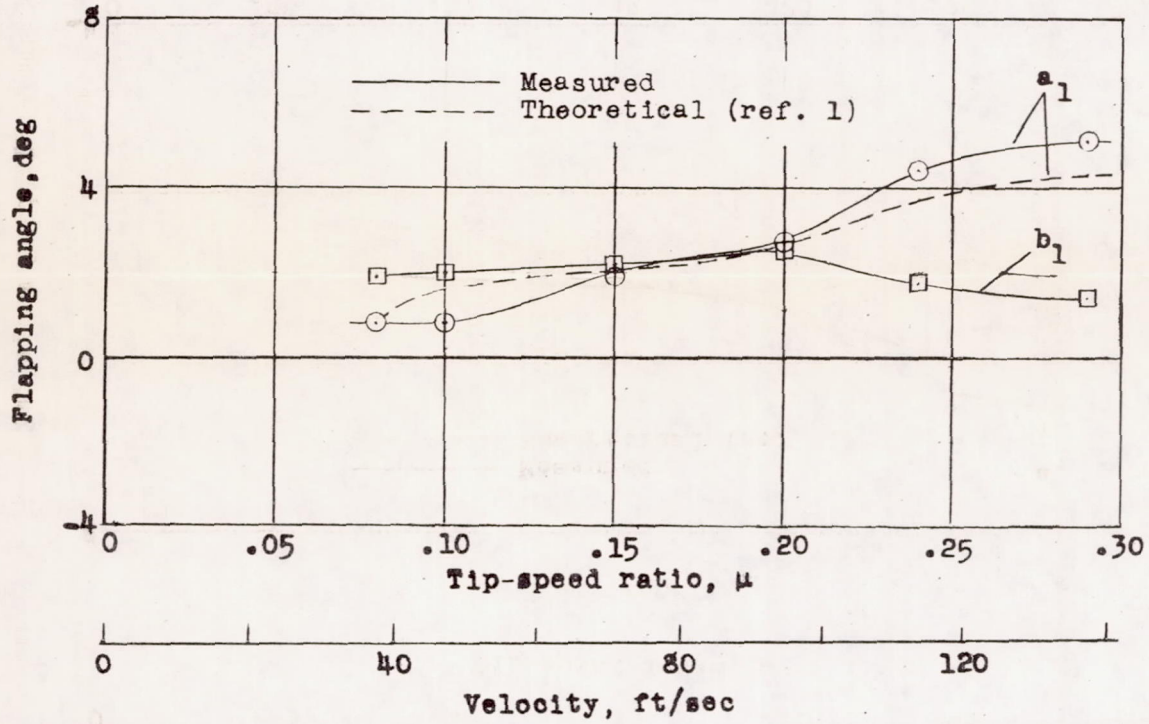

(b) Blade motions.

Figure 4.- Performance data.

NATIONAL ADVISORY COMMITTEE FOR AERONAUTICS

RESEARCH MEMORANDUM

EXPERIMENTAL INVESTIGATION OF THE AERODYNAMIC LOADING ON A HELICOPTER ROTOR BLADE IN FORWARD FLIGHT

By John P. Rabbott, Jr., and Gary B. Churchill

SUMMARY

An experimental investigation of the aerodynamic loading on one blade of a two-blade teetering rotor has been conducted in forward flight for a tip-speed-ratio range of 0.08 to 0.29 at a disk loading of about 2.4 pounds per square foot and a tip speed of about 480 feet per second. Chordwise loading distributions at five spanwise stations and the variation of section loading and total blade lift with azimuth position are presented. Also determined are the harmonic content and phase angles of section and total blade lift for the first six harmonics of rotor speed. The data show a much greater harmonic content, which, in general, varies inversely with tip-speed ratio for the range of tip-speed ratios investigated, than a uniform inflow theory would predict. The nondimensional spanwise loading is indicated to be relatively constant with thrust coefficient and tip-speed ratio.

INTRODUCTION

A knowledge of the chordwise and spanwise aerodynamic loading distribution on a helicopter rotor blade is often required to predict possible sources of vibration excitation which lead to stress and fatigue problems in the rotor system.

Although present rotor theory (refs. 1 and 2) predicts the overall rotor thrust and power required sufficiently well, it does not, in general, indicate the presence of appreciable higher harmonic air loads above the second harmonic, inasmuch as a uniform induced velocity across the rotor disk is usually assumed. Because of the very complex nature of the flow in a rotor wake, the calculation of the actual induced flow pattern is a very difficult mathematical problem. However, there are recent theories available, such as those of references 3 and 4, which more closely approximate the actual induced velocity distribution than does a simple uniform inflow assumption.

In a previous experimental investigation of rotor-blade loading (ref. 5), the aerodynamic loading on a model rotor blade was determined

for a wide variety of flight conditions but did not indicate harmonic loads above the second harmonic because of the low frequency response of the measuring equipment.

In order to provide the designer with a more quantitative view of rotor-blade loading than calculations or previous measurements would indicate, an investigation has been conducted in the Langley full-scale tunnel to measure the chordwise and spanwise aerodynamic loading distribution on a helicopter rotor blade in static thrust and forward flight. The static-thrust results are presented in reference 6, and the present paper covers the forward-flight data. Test conditions, which were all below stall in simulated level flight, correspond to a range of tip-speed ratios of 0.08 to 0.29 for a disk loading of about 2.4 pounds per square foot and a rotational tip speed of about 480 feet per second.

Differential pressures between the upper and lower surfaces were measured at ten chordwise locations for five spanwise stations at each test condition. The data were reduced to give chordwise and spanwise loading distributions and the variation of section and total blade load with azimuth. The latter data were then harmonically analyzed to give the amplitudes and phase angles of section and total load for the first six harmonics of rotor speed. These data are presented and a comparison is made with the loading predicted on the basis of an assumed uniform inflow. Rotor forces, shaft torque, and blade motions were also measured and are presented herein.

SYMBOLS

a' projection of angle between rotor force vector and axis of no feathering in plane containing flight path and axis of no feathering

a_1 coefficient of $\cos \psi$ in Fourier series for blade flapping; longitudinal flapping angle, deg

b_1 coefficient of $\sin \psi$ in Fourier series for blade flapping; lateral flapping angle, deg

b number of blades

c blade section chord, ft

c_l section lift coefficient, Lift/qc

C_T thrust coefficient, $\frac{T}{\pi R^2 \rho (\Omega R)^2}$

D	drag, lb
f	equivalent flat-plate area representing parasite drag, based on unit drag coefficient, $\frac{\text{Helicopter parasite drag}}{\frac{1}{2}\rho V^2}$, sq ft
l	instantaneous section lift, lb
l_o	steady term in series for section lift, lb/in.
l_n	coefficient of $\cos(n\psi + \phi_n)$ in series for section lift, lb/in.
L	instantaneous total blade lift, lb
L_o	steady term in series for total blade lift, lb
L_n	coefficient of $\cos(n\psi + \Phi_n)$ in series for total blade lift, lb
n	harmonic order
q	local dynamic pressure, lb/sq ft
r	radial distance to blade element, ft
R	blade radius measured from center of rotation, ft
T	rotor thrust, lb
v	induced inflow velocity at rotor, ft/sec
v_o	momentum value of induced velocity in hovering, $\Omega R\sqrt{\frac{C_T}{2}}$, ft/sec
V	forward velocity, ft/sec
x	distance from leading edge to any point on chord, ft
α	rotor angle of attack; angle between projection in plane of symmetry of axis of no feathering and line perpendicular to flight path, positive rearward, deg
α_r	blade-element angle of attack, measured from line of zero lift, deg
θ	blade-section pitch angle; angle between line of zero lift of blade section and plane perpendicular to axis of no feathering, deg

λ inflow ratio, $\frac{(V \sin \alpha - v)}{\Omega R}$

μ tip-speed ratio, $\frac{V \cos \alpha}{\Omega R}$

ρ mass density of air, slugs/cu ft

σ rotor solidity, $\frac{bc}{\pi R}$

ϕ_n phase angle, with respect to zero azimuth, of amplitude of nth harmonic of section lift, deg

Φ_n phase angle, with respect to zero azimuth, of amplitude of nth harmonic of total blade lift, deg

ψ blade azimuth angle measured from downwind position in direction of rotation, deg

Ω rotor angular velocity, radians/sec

DESCRIPTION OF EQUIPMENT

The equipment, with the exception of the blade-motion indicators, is described in detail in reference 6, but is reviewed briefly here.

Rotor Blades

The rotor blades are of rectangular plan form, untwisted, and have a diameter of approximately 15 feet, an NACA 0012 airfoil section, and a rotor solidity of 0.097. One blade of the two-blade teetering rotor is instrumented to measure the differential pressures between the upper and lower surfaces at ten chordwise locations at each of five spanwise stations. Figure 1 is a sketch of the instrumented blade showing the principal dimensions and the pressure-orifice locations. Figure 2 shows the details of the teetering rotor hub.

The rotor-blade stiffness, both in bending and in torsion, is very high. The bending stiffness varies from a maximum of about 9,000,000 pounds per square inch at the root to a constant value of 2,850,000 pounds per square inch for the outboard 40 percent of the blade span. The overall torsional stiffness, measured between the blade root and blade tip, is 278 inch-pounds per degree of twist.

Pressure-Pickup Installation

The pressure pickups used are NACA miniature electrical pressure gages (ref. 7) of a variable-inductance type. Fifty gages are mounted inside the rotor blade in such a way that neither centrifugal force nor flapping accelerations affect gage output. Inasmuch as the rotor is of the teetering type (without drag hinges), there can be no appreciable in-plane motion to affect the gages. A short length of tubing connects each gage to the appropriate pair of orifices. The tubing diameter and length are constant for all gages in order to maintain constant amplitude and phase response between gages. The amplitude and phase response for the measuring system, including the oscillograph on which the pressure data were recorded, were calibrated. The overall frequency response for the system was determined to be flat to about 60 cycles per second, the sixth harmonic of rotor speed. There was a time lag in the system, independent of frequency, which amounted to 8° of azimuth. Therefore, this lag is 16° for the second harmonic, 24° for the third harmonic, and so forth.

Although 45 slip rings were available for electrical connection between the rotating and stationary parts of the model, this number was not sufficient to enable all five pressure stations to be recorded at one time. Therefore, a remotely operated stepping switch, located on the rotor hub, was employed whereby stations 1, 2, and 3 (at $r/R = 0.31$, 0.56, and 0.75, respectively) were recorded simultaneously. The switch was then advanced and stations 3, 4, and 5 (at $r/R = 0.75$, 0.85, and 0.95, respectively) were recorded. Station 3 was thus recorded twice at each test point as a check on the repeatability of the data.

Blade-Motion Indicators

Blade pitch angles and flapping angles were measured by small variable transformers mounted on the rotor hub, as shown in figure 2. An input power of 400 cycles was used for each pickup and the output was filtered to give a single sine-wave trace with amplitude proportional to pitch angle or flapping angle. The response of the system was flat over the operating range. However, there was a time lag which varied with frequency and which was accounted for in the data-reduction process. Although reliable data were obtained, this system is not recommended for future work because of the complicated calibration and data-reduction methods required.

Test Vehicle and Wind Tunnel

Figure 3 shows the model in operation in the Langley full-scale tunnel. The rotor forces are transmitted through the shielded struts to the wind-tunnel balance. A complete description of the wind tunnel and its equipment

is given in reference 8. The torque input was measured by means of a strain-gage beam mounted on the rotor shaft.

TEST PROCEDURE AND DATA REDUCTION

In order to obtain the force tares on the basic model, the model was operated with blades off for the range of tunnel speeds and shaft angles of attack to be covered in the tests. Lift, drag, side force, and shaft torque tares were recorded. Then, in order to simulate a given flight condition for a given tunnel speed and rotor speed, the desired thrust and parasite drag were set and the side forces trimmed approximately to zero, the model tare forces being taken into account. Oscillograph records were taken of the pressure data and blade motions. The shaft torque was recorded on a potentiometer. Each oscillograph trace corresponding to the output of a pressure gage was read at 48 points per cycle. The readings for corresponding points for 10 cycles were averaged and recorded on automatic punch cards. Automatic computing machines then converted this average to a pressure differential and summed the output at each spanwise station to give the section loading. The section loading was then harmonically analyzed to give the amplitude and phase angle, with respect to zero azimuth, of each harmonic of loading. A correction for the time lag in the instrumentation described previously was then introduced. The values of section loading, when plotted against radius, were manually integrated to give total blade lift at 24 points per cycle. These data were then harmonically analyzed to give the amplitude and phase angle of each harmonic of total blade lift.

A similar analysis, for eight points per cycle, was made of the blade-motion traces, except that the sine and cosine components of the harmonic motions, corresponding to longitudinal and lateral blade flapping and pitch angles, respectively, were obtained.

The tunnel jet-boundary correction was assumed to be zero inasmuch as the tunnel configuration, with a ground plane installed, is similar to that described in reference 9 which showed the correction to be negligible. A stream-angle correction was applied to the rotor angles of attack.

RESULTS AND DISCUSSION

Performance Data

As discussed previously, the model force tares were measured and accounted for in setting the desired rotor forces at each test condition. Comparison of the drag tares thus obtained with those measured on the

same model in a previous investigation showed a large variation. Inasmuch as the balance parasite-drag values, therefore, were in doubt, the rotor parasite-drag—lift ratios for performance calculations were taken to be

$$\left(\frac{D}{L_o}\right)_p = -\tan(\alpha + a')$$

where α, the control axis angle of attack, was obtained from measured blade motions and a' was computed from reference 10. Table I shows a discrepancy between the rotor disk load obtained from the wind-tunnel balance and that obtained from integrated pressure data. The difference is less than 2 percent at $\mu = 0.10$, 0.15, and 0.20 but varies from 6 to 11 percent at the other three tip-speed ratios. This difference is similar to that discussed in reference 6, in that the integrated pressure lift is always less than the tunnel-balance lift for the thrust coefficients covered in this test. The tunnel-balance lift was used in performance calculations.

Figure 4(a) presents a comparison of the measured rotor power required with that calculated from references 1, 10, and 11. The shapes of the measured and theoretical curves are similar and the magnitudes agree fairly well, a maximum difference of about 8 percent occurring at $\mu = 0.15$.

Figure 4(b) presents a comparison of the blade flapping angles measured at the rotor hub with the calculated values of reference 1. The longitudinal flapping a_1 shows fair agreement. For an unconed teetering rotor, as used in this test, with uniform inflow, theory predicts no lateral flapping b_1, whereas the measurements show an appreciable value. A longitudinal variation in induced velocity, as discussed in reference 12, or blade bending would produce some lateral flapping.

No higher harmonics of blade flapping were measured greater than 0.1°, which is within the accuracy of the measuring equipment.

Section Aerodynamic Loading

Chordwise loading distribution.- Figure 5 presents sample chordwise loading distributions obtained at a tip-speed ratio of 0.29 for several azimuth positions. The curves, in general, are similar to those that would be expected from two-dimensional tests or theory, with the exception of $r/R = 0.95$. Here, over the rear part of the disk, the loading on the rear portion of the chord becomes negative. In reference 6 (static-thrust results) a similar effect was noted in that the trailing-edge loading at $r/R = 0.95$ was lower than two-dimensional data would show. This lower

value of loading was attributed to a possible spanwise boundary-layer growth due to rotation which added to the expected reduction in lift due to tip effects. Since reference 6 has been published, two-dimensional tests of the instrumented rotor blade have been made in the Langley low-turbulence pressure tunnel. Figure 6 shows some sample results from these tests. Figure 6, which is similar to figure 7 of reference 6, compares the measured chordwise loading in static thrust with the measured two-dimensional data and theoretical loadings. At $r/R = 0.75$ (fig. 6(a)), which is representative of inboard stations, good agreement between the three loading distributions indicates that approximately two-dimensional flow exists in this region. For $r/R = 0.95$ (fig. 6(b)), the two-dimensional measurements agree very well with the calculated loading distribution for the NACA 0012 profile. However, the trailing-edge loading is considerably lower for the static-thrust tests, as discussed in reference 6.

In order for this decreased trailing-edge loading to be a spanwise flow effect, a similar effect would be expected to be most pronounced in forward flight over the rear portion of the rotor disk where the forward-speed component would add to any radial flow present. Similarly, over the forward portion of the disk, the forward-speed component, directed radially inboard, would tend to minimize any radial flow due to rotation. This trend is seen in figure 5(e) at $r/R = 0.95$.

The main effect of such a chordwise loading change from two-dimensional results would be to introduce a possible periodic blade twist in a torsionally flexible rotor blade, which might not be accounted for in design calculations. Although it is believed that the section lift characteristics can be accurately obtained with the present instrumentation, it is felt that more chordwise pressure orifices, particularly in the trailing-edge region, would be required to determine definitely the variation in section pitching moment with azimuth.

Variation of section aerodynamic loading with azimuth.- Figure 7 presents the variation in section aerodynamic loading with azimuth for the five radial stations for a range of tip-speed ratios. As described in the section entitled "Description of Equipment," the data at $r/R = 0.75$ were taken twice. Both sets of data points are presented in order to give an indication of the repeatability of the data.

The main effects to be noticed are the harmonic content and the change in shape of the curves with tip-speed ratio. Consider first the outboard stations ($r/R = 0.75$, 0.85, and 0.95). At a tip-speed ratio of 0.08, (fig. 7(a)), which corresponds to a transition condition from hovering to forward flight where the induced-velocity dissymmetry is the greatest, the magnitude of the loading varies by a factor of 3 to 4, with sharp gradients in the regions of 90° and 270° of azimuth. The large gradients in loading suggest a relatively large harmonic content in this flight condition. At a greater forward speed, $\mu = 0.20$ (fig. 7(d)), the magnitude of the loading

variation with azimuth has decreased somewhat and the curves tend to smooth out over the retreating portion of the rotor disk.

At the highest tip-speed ratio, $\mu = 0.29$, a value which corresponds to a higher cruising speed but is still below stall, the inflow through the rotor is more nearly uniform because of the larger component of forward speed. This condition would suggest a less severe variation in lift, as the measured data show in figure 7(f). Although the magnitude of loading variation is still of the same order as at $\mu = 0.20$ (fig. 7(d)), it is now predominantly first and second harmonic in nature.

If the tip-speed ratio were increased to a point where retreating blade stall occurred, or if the forward-speed component were an appreciably greater part of the local dynamic pressure, higher harmonic loading would probably be evidenced again. No such data were obtained in the present tests, but these conditions should be covered in future investigations.

If the inboard stations ($r/R = 0.31$ and 0.56) are considered next, an opposite trend with tip-speed ratio is noted from that seen for the outboard stations. Inasmuch as the local blade lift is low at the inboard stations, particularly at $r/R = 0.31$, the induced velocity is correspondingly low and the variation in section lift is mainly due to changes in dynamic pressure, at a relatively constant section angle of attack. The local dynamic pressure can be expressed as

$$q = \frac{1}{2}\rho(\Omega R)^2\left(\frac{r}{R} + \mu \sin \psi\right)^2$$

At the low tip-speed ratios, $\mu \sin \psi$ is small compared with the radius term and the local dynamic pressure is mainly due to rotation, and, thus, is relatively constant. Therefore, the section lift is also relatively constant with azimuth as in figure 7(a). At the higher tip-speed ratios, the forward-speed component is appreciable and results in a greater change in lift with azimuth.

At the higher forward speeds, the blade flapping increases because of the greater rotor inflow and introduces a larger variation in lift than changes in local dynamic pressure alone would produce, as seen in figure 7(f).

In order to illustrate the effect of the inclusion of higher harmonic loadings having larger magnitudes than would be predicted by a standard theory for a uniform inflow (ref. 1), figure 8 gives a comparison of the measured variation in section loading with azimuth at $r/R = 0.75$ with the variation predicted by theory. The theoretical curve has been adjusted to give the same average load as the measured data in each case.

The blade section angle of attack for a teetering rotor can be expressed as in reference 1:

$$\alpha_r = \theta - a_1 \sin \psi + \frac{\lambda + \mu a_1}{\frac{r}{R} + \mu \sin \psi}$$

With the assumption of uniform inflow and zero coning angle, λ is constant for a given condition and no lateral flapping or second harmonic blade motion is predicted. Therefore, the longitudinal flapping and the local velocity mainly determine the variation in lift with azimuth. At a low tip-speed ratio (fig. 8(a)) where the flapping angle is small and the velocity relatively constant, the theoretical curve shows very little change in lift, whereas the measured data indicate the greatest variation. At the higher forward speeds, the theoretical curve approaches the measured data, inasmuch as both are predominantly second harmonic.

Harmonic content of section loading.- The harmonic content of the measured data can be seen in figure 9, which presents the harmonic amplitudes, in bar-graph form, of the data of figure 7. The dashed lines denote repeated data points at $r/R = 0.75$. Inasmuch as the variation in section lift is periodic in nature, it can be represented in harmonic-series form as

$$l = l_0 + \sum_{n=1}^{n} l_n \cos(n\psi + \phi_n)$$

This series is equivalent to the more common Fourier series expansion of a harmonic function

$$l = l_0 + \sum_{n=1}^{n} (A_n \cos n\psi + B_n \sin n\psi)$$

where

$$l_n = \sqrt{A_n^2 + B_n^2}$$

and

$$\phi_n = \tan^{-1}\left(-\frac{B_n}{A_n}\right)$$

where A_n and B_n are general Fourier series coefficients.

The ratio of the nth harmonic loading l_n to the steady component l_o, in percent, is presented in figure 9. The phase angles ϕ_n with respect to zero azimuth are presented in table II for each harmonic. When the results of figure 9 are interpreted, it should be noted that although the harmonic amplitudes are very large percentagewise for the most inboard station, $r/R = 0.31$, they represent a small force since the steady component is very small. This is particularly true at the high tip-speed ratios, where the steady load is nearly zero. However, this spanwise station could correspond to an antinode position and, therefore, could be important in a vibration analysis.

At the low tip-speed ratios, all harmonics through the sixth, in general, are appreciable and could be sources of vibration excitation for the helicopter components. These vibrations and the resulting fatigue would be most important for the load-lifter type of helicopter which normally operates at low tip-speed ratios. At tip-speed ratios above 0.2, the loading becomes predominantly first and second harmonic, the higher harmonics being only 2 to 5 percent of the average load, as in figure 9(f), where $\mu = 0.29$. Even at the high tip-speed ratios, however, if some lightly damped component of the helicopter is near resonance with a multiple of rotor speed, a source of vibration is present from the higher harmonic air loads.

Reference 13, which is an investigation of dynamic rotor-blade bending moments on a flight helicopter, shows a variation in harmonic bending-moment amplitudes with tip-speed ratio similar to the variation in blade loading indicated here.

During the data-reduction process several harmonics higher than the first six presented here were determined. Although some amplitude distortion is present above the sixth harmonic, the response of the system is relatively flat to the tenth harmonic; in this range, all harmonic loadings were appreciably smaller in magnitude than the sixth.

As discussed in the section entitled "Test Procedure and Data Reduction," the output of each pressure gage was read at 48 points per cycle for 10 cycles, and the corresponding points were averaged before the section loading and harmonic analyses were obtained. This method of analysis was done because some variation in output from cycle to cycle could be seen from an inspection of the oscillograph records. In order to check the validity of this procedure and to determine whether any variation in harmonic content with time was present, an analysis was made of three individual cycles for $r/R = 0.75$ at $\mu = 0.08$ for both the original and the check points. Cycles 1, 5, and 10 were analyzed for both conditions. The time interval between cycles considered was one-half second, and approximately 10 seconds elapsed between original and check points. An inspection of these results showed that the percentage harmonic amplitudes had a spread of ± 1 percent and the phase angles were within $\pm 15^\circ$.

Spanwise Loading Distribution

The spanwise loading distribution is given in figure 10 for several azimuth positions at three tip-speed ratios. Figure 10(a) is for $\mu = 0.08$, a transition condition, where the greatest variation in section loading with azimuth was found earlier. This figure shows that the spanwise loading distribution is also very irregular at this condition. The loading curves tend to smooth out with increasing forward speed, and at $\mu = 0.29$ (fig. 10(c)), where the magnitude of the rotor induced velocity is small compared with the total inflow, the spanwise loading distributions more nearly resemble those measured in static thrust, as given in reference 6.

A comparison of the data of figure 10 with the spanwise loading curves of reference 6 in static thrust indicates that a greater tip loss is evidenced in the forward-flight condition, as shown by the relatively lower loading at $r/R = 0.95$ compared with the more inboard stations.

Although the instantaneous spanwise loading distributions show a variation with tip-speed ratio, it can be shown that the steady-loading distribution is relatively constant.

In figure 11 the steady section loading is nondimensionalized by dividing by the average spanwise loading; that is, the quantity $\frac{l_o}{L_o/R}$ is plotted against r/R. Figure 11(a) for the present forward-flight data (for which there was no retreating tip stall) shows that the nondimensional steady-loading curves are constant within about 10 percent for a range of tip-speed ratios of 0.08 to 0.29 within a thrust-coefficient range of 0.00367 to 0.00482. A similar curve is shown in figure 11(b) for the static-thrust data of reference 6 covering a wider range of thrust coefficients from 0.00334 to 0.00599, all values being below stall.

As discussed in reference 6, the spanwise loading distribution near the blade tip is a function of thrust coefficient, because of tip-loss effects, which contribute to the scatter of the data at $r/R = 0.95$.

The section aerodynamic loading has been calculated at $r/R = 0.75$, a uniform induced velocity being assumed, for four thrust coefficients bracketing the measured data at a tip-speed ratio of 0.20. The resulting variation in lift with azimuth was harmonically analyzed, and the results are presented in table III. The amplitudes are given in nondimensional form, as in figure 9. The phase angles are given also. The table indicates that the theoretical harmonic amplitudes, in percent of average load, are essentially constant with thrust coefficient in forward flight. The phase angles are also approximately constant, the first and third harmonics showing the largest variance, inasmuch as the magnitudes of loading are small with a corresponding decrease in accuracy.

Therefore, until additional experimental data are available, the nondimensional harmonic loading given in figure 9 might tentatively be applied to rotor blades of similar configuration at different thrust coefficients. Some discussion is given in reference 6 of methods of calculating the spanwise aerodynamic loading distribution in static thrust which might be used as an approximation to the average forward-flight loading.

Total Blade Lift

The spanwise loading distributions at 24 azimuth positions were integrated to give total blade lift which is plotted against azimuth in figure 12 for a range of tip-speed ratios. The change in shape of these curves with tip-speed ratio is similar to the changes in the section loading data as discussed previously. The higher harmonics again are most apparent at the low forward speeds and decrease with increasing tip-speed ratio to a predominant second harmonic at the high tip-speed ratios.

The theoretical blade lift due to a uniform inflow is compared with the measured data in figure 12 for three tip-speed ratios. By the same reasoning discussed with the section loading data, at $\mu = 0.08$ the theory predicts very little variation in total lift with azimuth, where the measurements indicate the greatest variation. At $\mu = 0.20$ (fig. 12(d)), the theoretical amplitudes are approaching the measurements, although the harmonic content differs greatly and, at $\mu = 0.29$ (fig. 12(f)), where the magnitude of the rotor induced flow is small compared with the total inflow, the agreement between theory and experiment is fairly close. The measured lift is now predominantly second harmonic, as the theory predicts in all cases, and the amplitudes of loading are of the same order of magnitude.

The results of a harmonic analysis of the measured total blade lift are given in figure 13 and table IV. Figure 13 presents the harmonic amplitudes as a percent of the steady lift per blade, and table IV gives the corresponding phase angles. The variation in harmonic content of total blade lift with tip-speed ratio is seen to be less definite, except for the second harmonic, than was indicated for the section data.

The results of a harmonic analysis of the variation of theoretical blade lift with azimuth are given in table V for a tip-speed ratio of 0.20 and three thrust coefficients bracketing the measurements. This table shows that in forward flight the amplitudes of harmonic loading, as a percent of the steady load, and the phase angles are essentially constant with thrust coefficient for the total lift as well as the section loading discussed earlier.

Figure 14 presents the variation of root-mean-square harmonic amplitudes of total blade lift with the ratio of forward speed to the momentum

value of induced velocity in hovering. The root-mean-square amplitude is defined as

$$\sqrt{\frac{\left(\frac{L_1}{L_o}\right)^2 + \left(\frac{L_2}{L_o}\right)^2 + \cdots + \left(\frac{L_6}{L_o}\right)^2}{6}}$$

This quantity may be thought of as an overall average harmonic content of total blade lift. The root-mean-square amplitude appears to peak at a velocity ratio of about 2, corresponding to a tip-speed ratio of about 0.1, where the higher harmonics predominate. The curve then decreases to a minimum at about $V/v_o = 4$ (a tip-speed ratio of about 0.2) as the higher harmonics decrease in magnitude and increases thereafter to the highest forward speed investigated as the second harmonic loading becomes increasingly larger.

The variation of aerodynamic moment about the flapping hinge with azimuth was determined for one flight condition, $\mu = 0.08$. These data were harmonically analyzed and showed that there was no appreciable first harmonic aerodynamic moment, as is to be expected for a rotor with a zero-offset flapping hinge.

Rotor-Disk Load Distribution

An overall view of the changes in rotor-disk load distribution with forward speed can be seen in figure 15 where section loading in pounds per inch is plotted in contour form over the rotor disk, for a range of tip-speed ratios. As with the data previously discussed, the contour loading shows the greatest nonuniformity at the lowest tip-speed ratio and becomes relatively smoother at the high tip-speed ratios. The region of maximum loading also changes with forward speed, shifting from the front to the rear of the rotor disk with increasing tip-speed ratio.

The sharp loading changes in the region of 0° azimuth in figures 15(b), 15(c), and 15(d) may be attributable to the effects of the wake of the rotor hub.

CONCLUSIONS

The results of an experimental investigation of the chordwise and spanwise aerodynamic loading distribution on a two-blade untwisted teetering helicopter rotor blade in simulated level flight for a range of tip-speed

ratios of 0.08 to 0.29 at a disk load of about 2.4 pounds per square foot and a tip speed of 480 feet per second lead to the following conclusions:

1. The chordwise loading distributions are, in general, conventional in appearance; however, a low or negative loading on the rear portion of the blade chord at the 95-percent-radius station is found over the rear of the rotor disk. This condition is possibly caused by a spanwise boundary-layer growth due to rotation which adds to the expected decreased loading due to tip effects.

2. The variation of section loading and total blade lift with azimuth shows a much larger harmonic content than a uniform-inflow theory would predict. The first and second harmonics tend to increase with tip-speed ratio, whereas the third to sixth decrease for the range of tip-speed ratios tested.

3. The spanwise aerodynamic loading distributions are irregular in shape at low tip-speed ratios but become smoother at increased forward speeds where the magnitude of the rotor induced flow is smaller compared with the total inflow.

4. The nondimensional spanwise loading is indicated to be relatively constant with thrust coefficient and tip-speed ratio; this result suggests the possibility of extending the present results to rotors of similar configuration at other thrust coefficients below stall.

5. The root-mean-square harmonic amplitudes of total blade lift peak in the transition region, decrease somewhat at a moderate cruise condition, and then increase again to the highest forward speed covered in the tests.

6. The contours of loading over the rotor disk are also found to become more uniform as tip-speed ratio increases. Peak loading position shifts from the front to the rear of the disk with increasing tip-speed ratio.

Langley Aeronautical Laboratory,
National Advisory Committee for Aeronautics,
Langley Field, Va., August 3, 1956.

REFERENCES

1. Bailey, F. J., Jr.: A Simplified Theoretical Method of Determining the Characteristics of a Lifting Rotor in Forward Flight. NACA Rep. 716, 1941.

2. Gessow, Alfred, and Crim, Almer D.: An Extension of Lifting Rotor Theory To Cover Operation at Large Angles of Attack and High Inflow Conditions. NACA TN 2665, 1952.

3. Castles, Walter, Jr., and DeLeeuw, Jacob Henri: The Normal Component of the Induced Velocity in the Vicinity of a Lifting Rotor and Some Examples of Its Application. NACA Rep. 1184, 1954. (Supersedes NACA TN 2912.)

4. Heyson, Harry H., and Katzoff, S.: Normal Component of Induced Velocity in the Vicinity of a Lifting Rotor With a Nonuniform Disk Loading. NACA TN 3690, 1956.

5. Meyer, John R., Jr., and Falabella, Gaetano, Jr.: An Investigation of the Experimental Aerodynamic Loading on a Model Helicopter Rotor Blade. NACA TN 2953, 1953.

6. Rabbott, John P., Jr.: Static-Thrust Measurements of the Aerodynamic Loading on a Helicopter Rotor Blade. NACA TN 3688, 1956.

7. Patterson, John L.: A Miniature Electrical Pressure Gage Utilizing a Stretched Flat Diaphragm. NACA TN 2659, 1952.

8. DeFrance, Smith J.: The N.A.C.A. Full-Scale Wind Tunnel. NACA Rep. 459, 1933.

9. Silverstein, Abe, and Katzoff, S.: Experimental Investigation of Wind-Tunnel Interference on the Downwash Behind an Airfoil. NACA Rep. 609, 1937.

10. Amer, Kenneth B., and Gustafson, F. B.: Charts for Estimation of Longitudinal-Stability Derivatives for a Helicopter Rotor in Forward Flight. NACA TN 2309, 1951.

11. Bailey, F. J., Jr., and Gustafson, F. B.: Charts for Estimation of the Characteristics of a Helicopter Rotor in Forward Flight. I - Profile Drag-Lift Ratio for Untwisted Rectangular Blades. NACA WR L-110, 1944. (Formerly NACA ACR L4H07.)

12. Migotsky, Eugene: Full-Scale Investigation of the Blade Motion of the PV-2 Helicopter Rotor. NACA TN 1521, 1948.

13. Daughaday, H., and Kline, J.: An Approach to the Determination of Higher Harmonic Rotor Blade Stresses. Rep. No. CAL-52, Cornell Aero. Lab., Inc., Mar. 1953.

TABLE I.- SUMMARY OF TEST CONDITIONS

Tip-speed ratio, μ	Disk load, lb/sq ft		ΩR, ft/sec	Thrust coefficient		α, deg	f, sq ft
	Balance data	Rotor pressure measurements		Balance data	Rotor pressure measurements		
0.08	2.20	2.06	492	0.00393	0.00367	-1.1	---
.10	2.44	2.41	482	.00446	.00440	-1.9	2.8
.15	2.41	2.38	462	.00487	.00482	-4.0	2.5
.20	2.47	2.43	482	.00467	.00460	-6.8	3.1
.24	2.57	2.36	487	.00476	.00436	-9.8	3.2
.29	2.44	2.16	483	.00445	.00394	-11.7	2.7

TABLE II.- PHASE ANGLE FOR EACH HARMONIC

OF MEASURED SECTION LOADING

Tip-speed ratio, μ	n	Phase angle, ϕ_n, deg, for station -					
		1	2	3	3 (repeat)	4	5
0.08	1	-12	2	194	193	174	185
	2	-2	-20	1	-3	12	148
	3	45	78	-125	-118	-15	-12
	4	97	156	193	182	182	8
	5	159	143	97	65	181	194
	6	236	127	153	145	25	192
.10	1	-13	-1	177	178	166	183
	2	-3	-7	-6	-4	22	110
	3	192	26	1	-36	-17	-2
	4	208	162	162	160	187	-25
	5	198	129	1	7	159	194
	6	204	158	151	140	23	175
.15	1	-56	10	-109	-15	102	107
	2	1	-15	5	6	23	54
	3	-42	122	-15	-15	-6	4
	4	-81	-33	197	179	-86	-25
	5	53	-104	131	126	171	188
	6	-23	119	-28	-27	123	172
.20	1	-91	-134	-41	-56	-2	132
	2	-3	-5	5	10	39	24
	3	-128	-53	-19	-17	5	-3
	4	-80	-120	-110	-120	-84	-31
	5	249	-7	128	137	165	161
	6	29	248	75	81	126	183
.24	1	189	-61	-47	-45	19	52
	2	45	-4	2	3	17	-20
	3	187	-106	-33	-34	-92	-47
	4	176	189	-107	-101	-76	-20
	5	224	64	143	131	216	32
	6	202	-38	56	61	154	117
.29	1	-158	-45	-24	-29	16	49
	2	35	9	5	4	14	-16
	3	226	-130	-13	-24	-133	-18
	4	174	171	-109	-103	-107	-17
	5	-97	106	174	140	-22	27
	6	211	67	79	65	114	-48

TABLE III.- HARMONIC ANALYSIS OF THEORETICAL SECTION LIFT

[μ = 0.20; ΩR = 482 ft/sec; f = 2.2 sq ft; r/R = 0.75]

C_T	Disk loading, lb/sq ft	$\frac{l_1}{l_0}$	ϕ_1, deg	$\frac{l_2}{l_0}$	ϕ_2, deg	$\frac{l_3}{l_0}$	ϕ_3, deg
0.00223	1.23	0.021	-89	0.142	-2	0.007	-108
.00335	1.85	.012	-88	.131	0	.016	-101
.00447	2.47	.015	-92	.126	0	.010	-98
.00734	4.05	.005	-112	.125	0	.012	-82

TABLE IV.- PHASE ANGLE FOR EACH HARMONIC

OF MEASURED TOTAL BLADE LIFT

Tip-speed ratio, μ	Φ_1, deg	Φ_2, deg	Φ_3, deg	Φ_4, deg	Φ_5, deg	Φ_6, deg
0.08	-13	1	-5	165	173	129
.10	-6	2	-9	162	137	108
.15	-20	-5	0	-97	146	114
.20	-51	6	-15	-90	144	166
.24	-8	4	-123	-120	172	-27
.29	-14	8	-124	-175	127	144

TABLE V.- HARMONIC ANALYSIS OF THEORETICAL TOTAL BLADE LIFT

[μ = 0.20; ΩR = 482 ft/sec; f = 2.2 sq ft]

C_T	Disk loading, lb/sq ft	L_1/L_o	Φ_1, deg	L_2/L_o	Φ_2, deg	L_3/L_o	Φ_3, deg
0.00223	1.24	0.023	90	0.144	0	0.028	-90
.00447	2.47	.007	-90	.118	0	.024	-90
.00761	4.20	.004	-84	.125	0	.022	-90

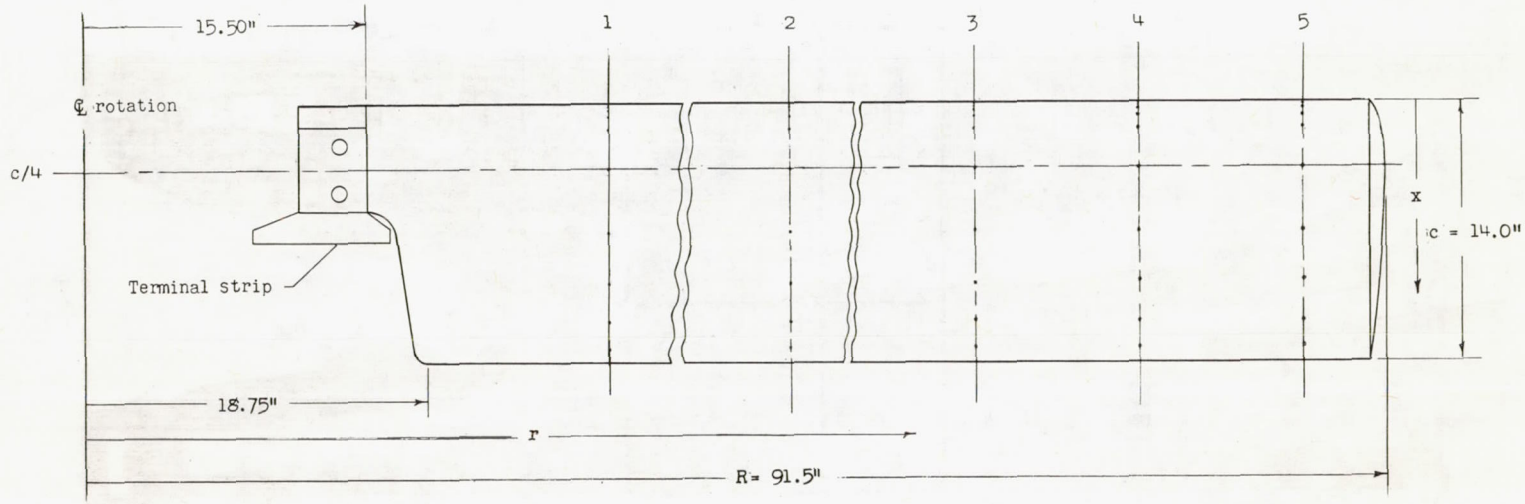

Chordwise station	x/c
1	0.005
2	.010
3	.025
4	.050
5	.100
6	.250
7	.500
8	.700
9	.850
10	.950

Radial station	r/R
1	0.31
2	.56
3	.75
4	.88
5	.95

Figure 1.- Blade layout showing location of pressure orifices. Airfoil section, NACA 0012; rotor solidity, $\sigma = 0.097$.

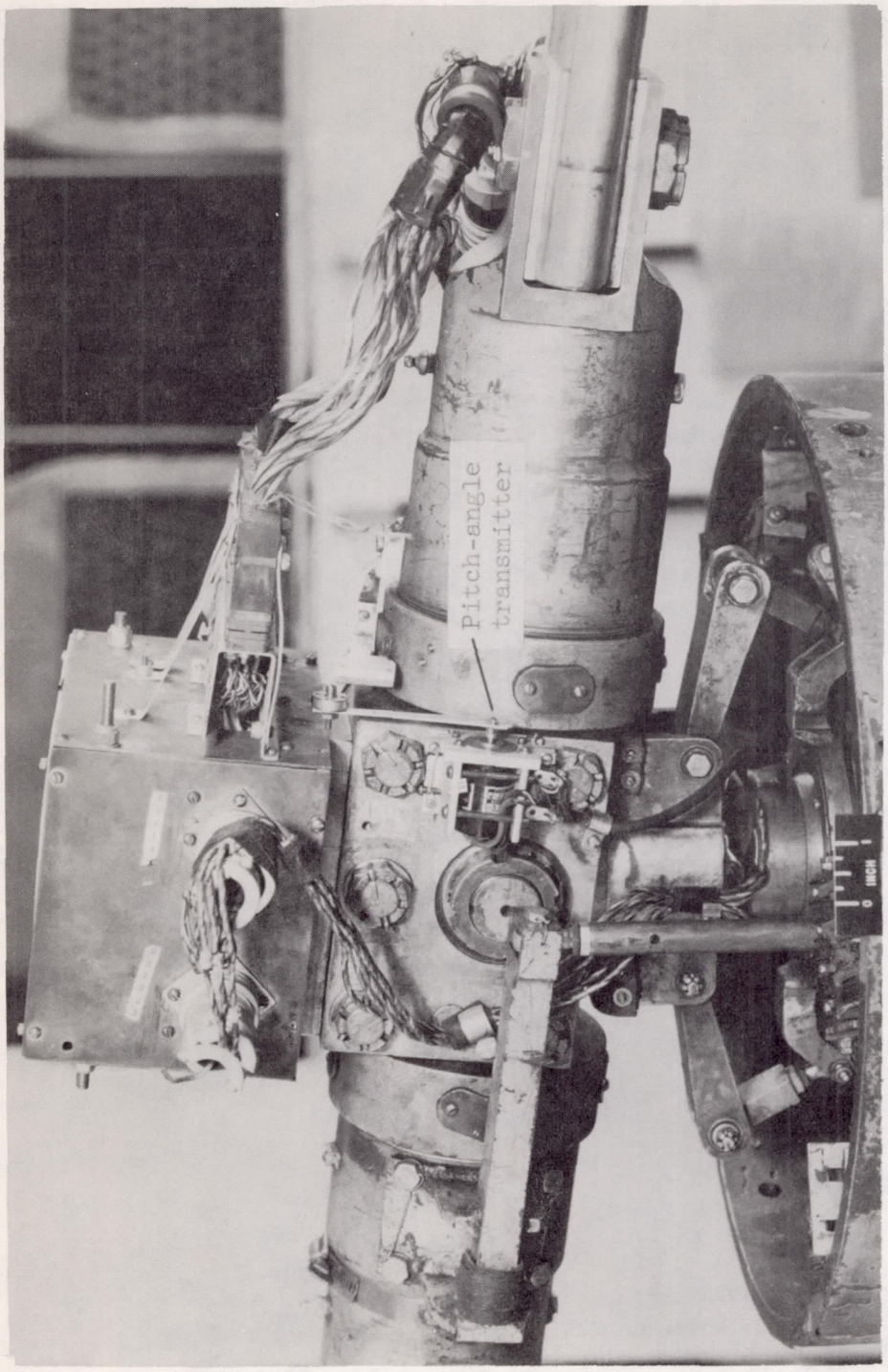

L-89201.1

Figure 2.- Detailed view of hub.

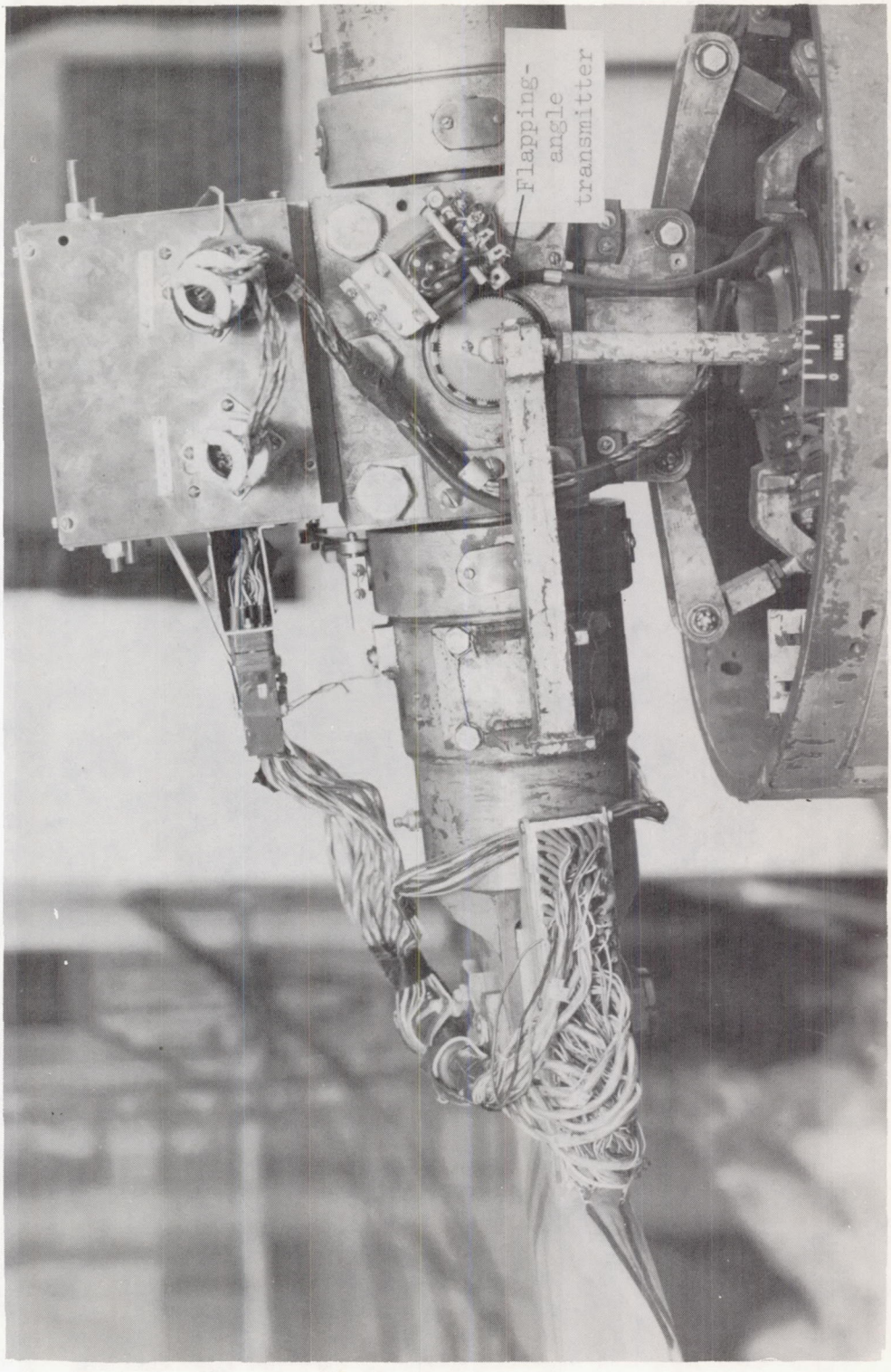

L-89202.1

Figure 2.- Concluded.

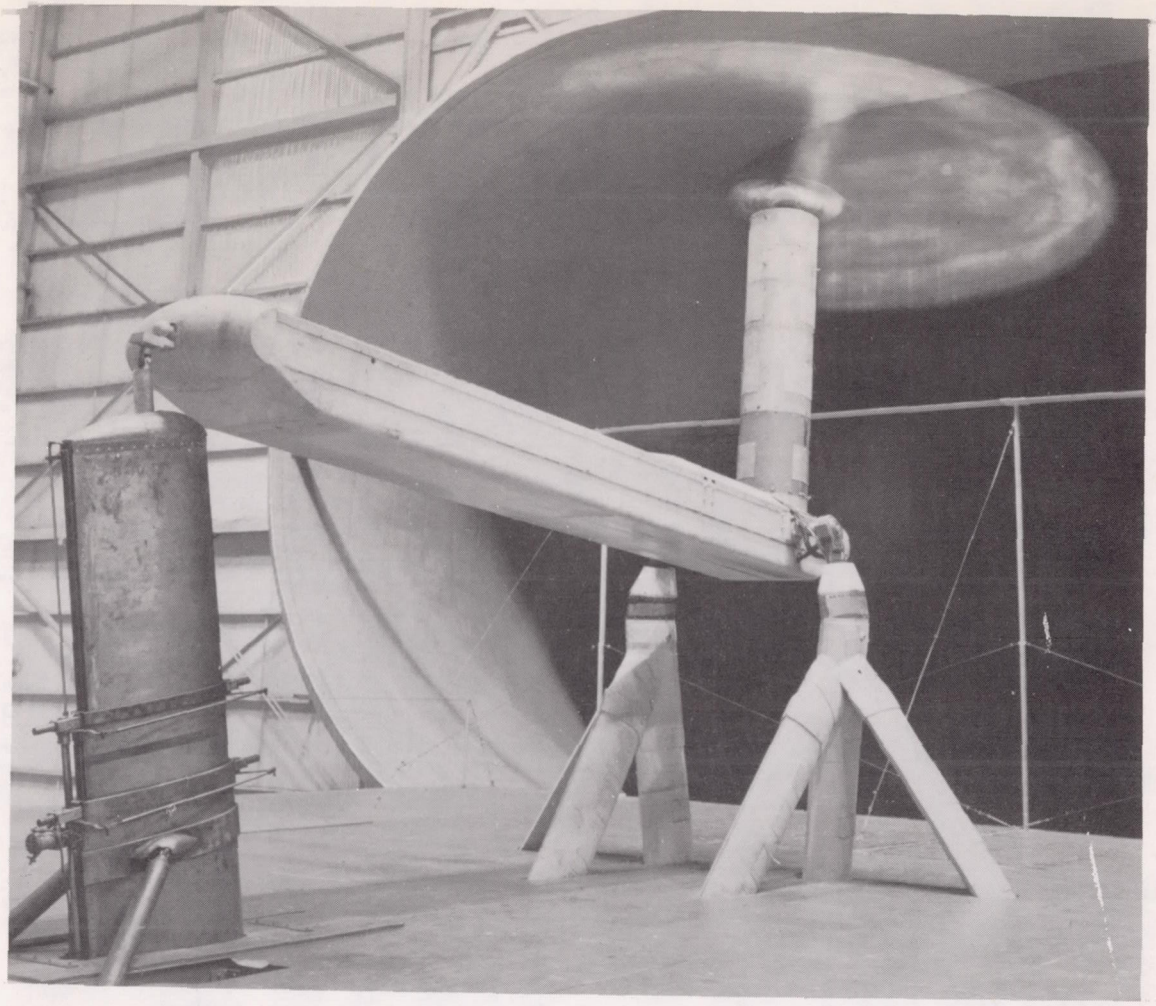

L-83264.2

Figure 3.- General view of model in Langley full-scale tunnel.

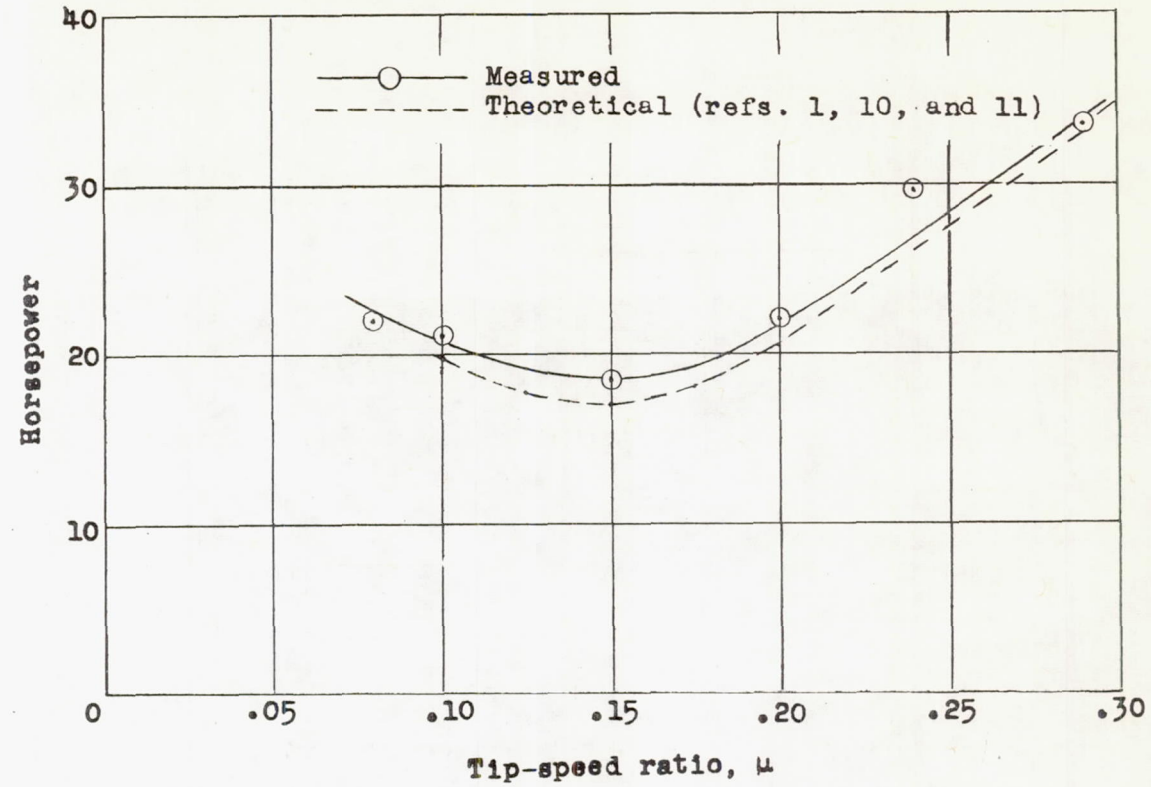

(a) Power required.

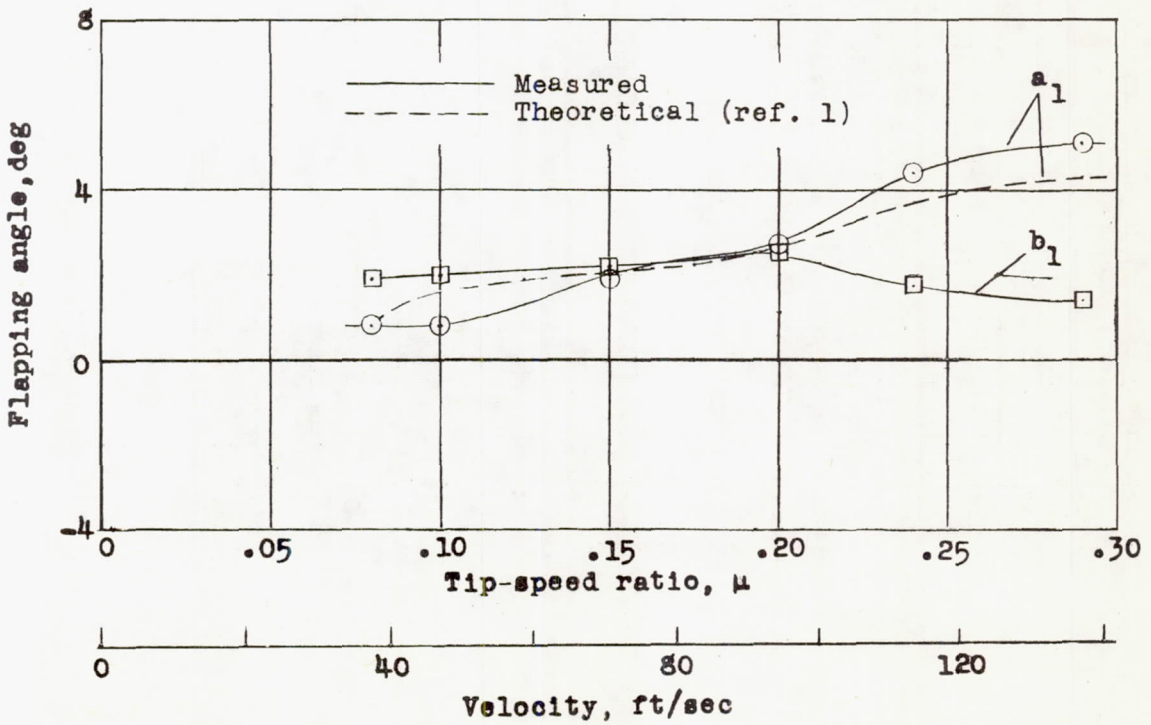

(b) Blade motions.

Figure 4.- Performance data.

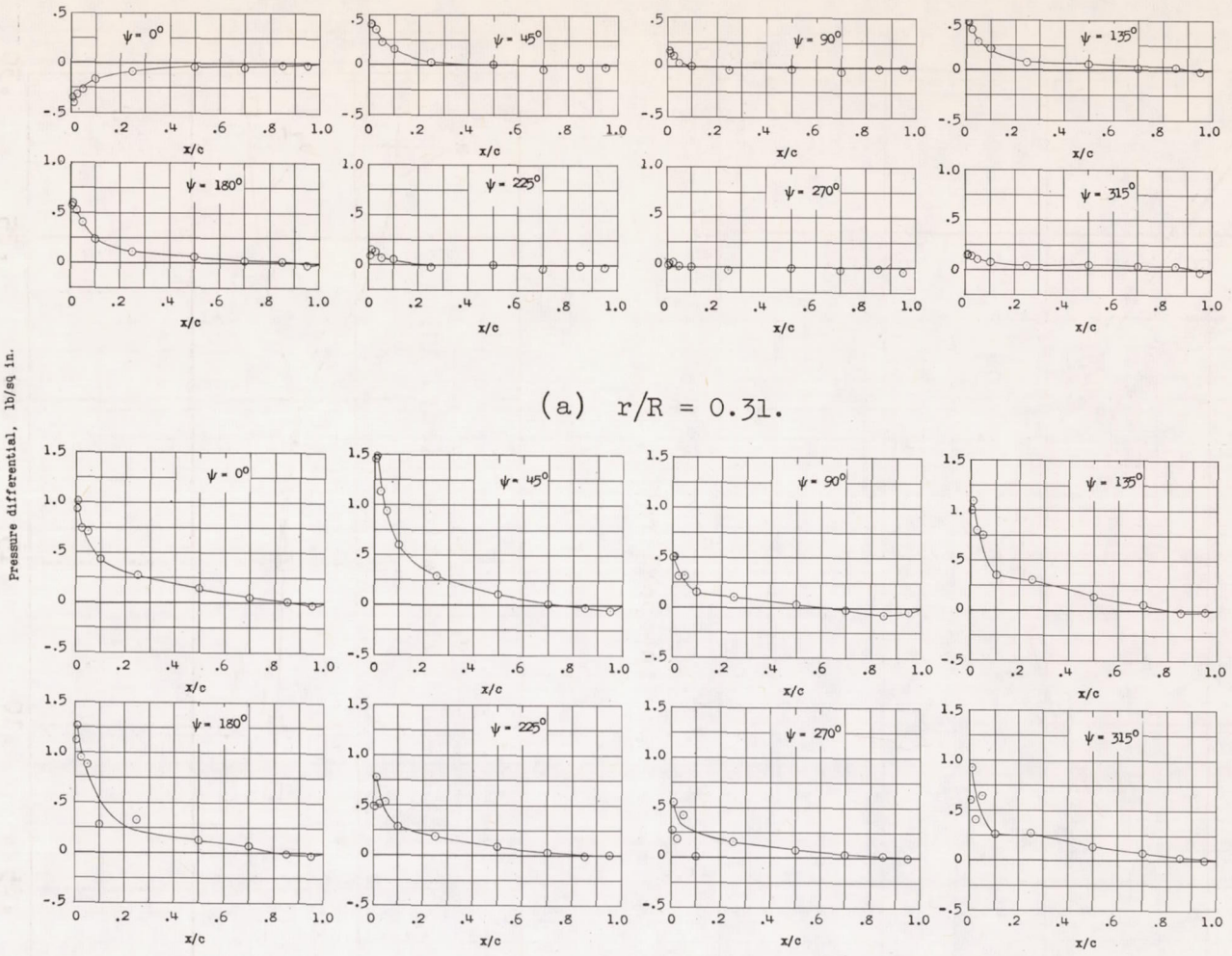

(a) r/R = 0.31.

(b) r/R = 0.56.

Figure 5.- Representative chordwise loading distributions at several azimuth positions. $\mu = 0.29$.

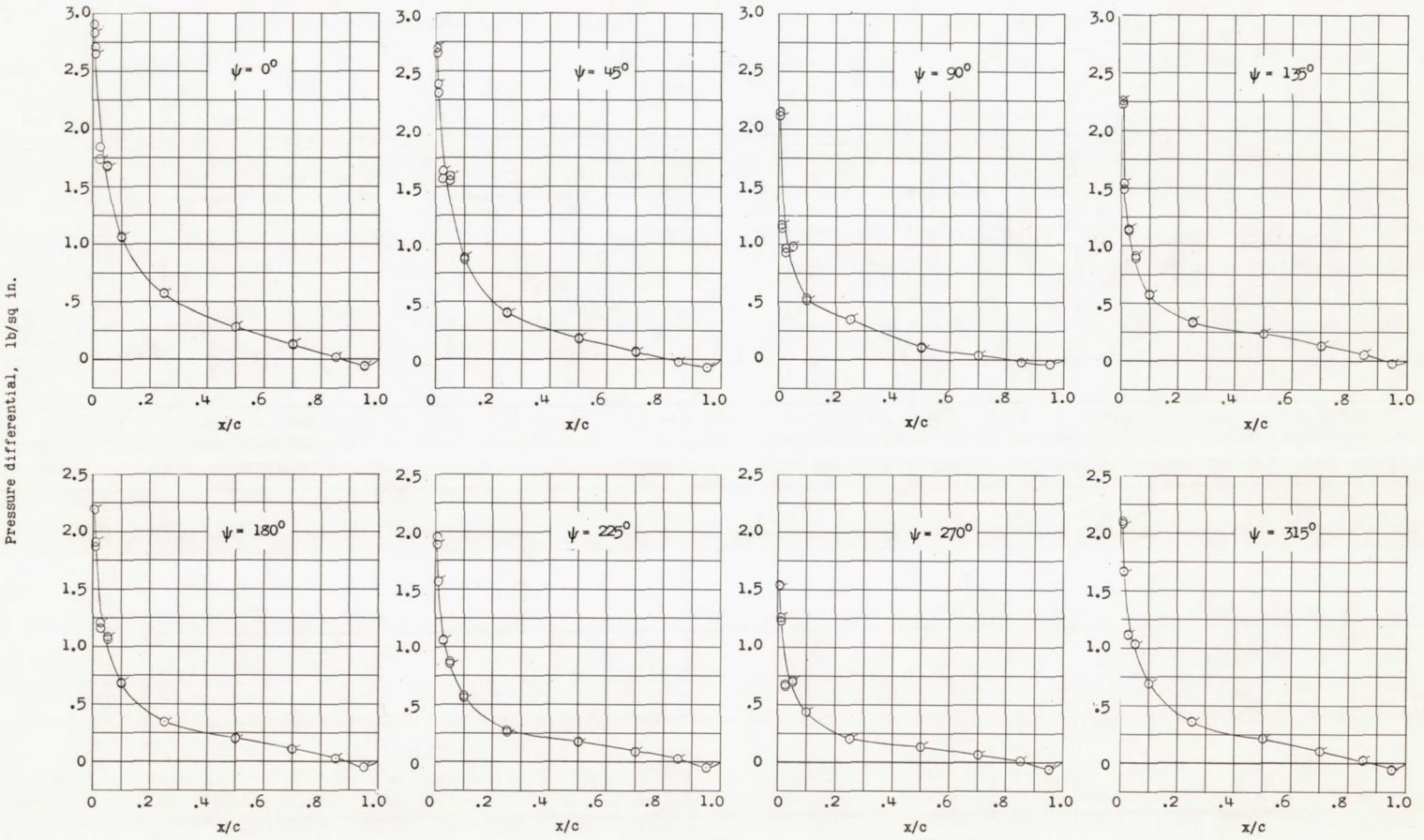

(c) r/R = 0.75.

Figure 5.- Continued.

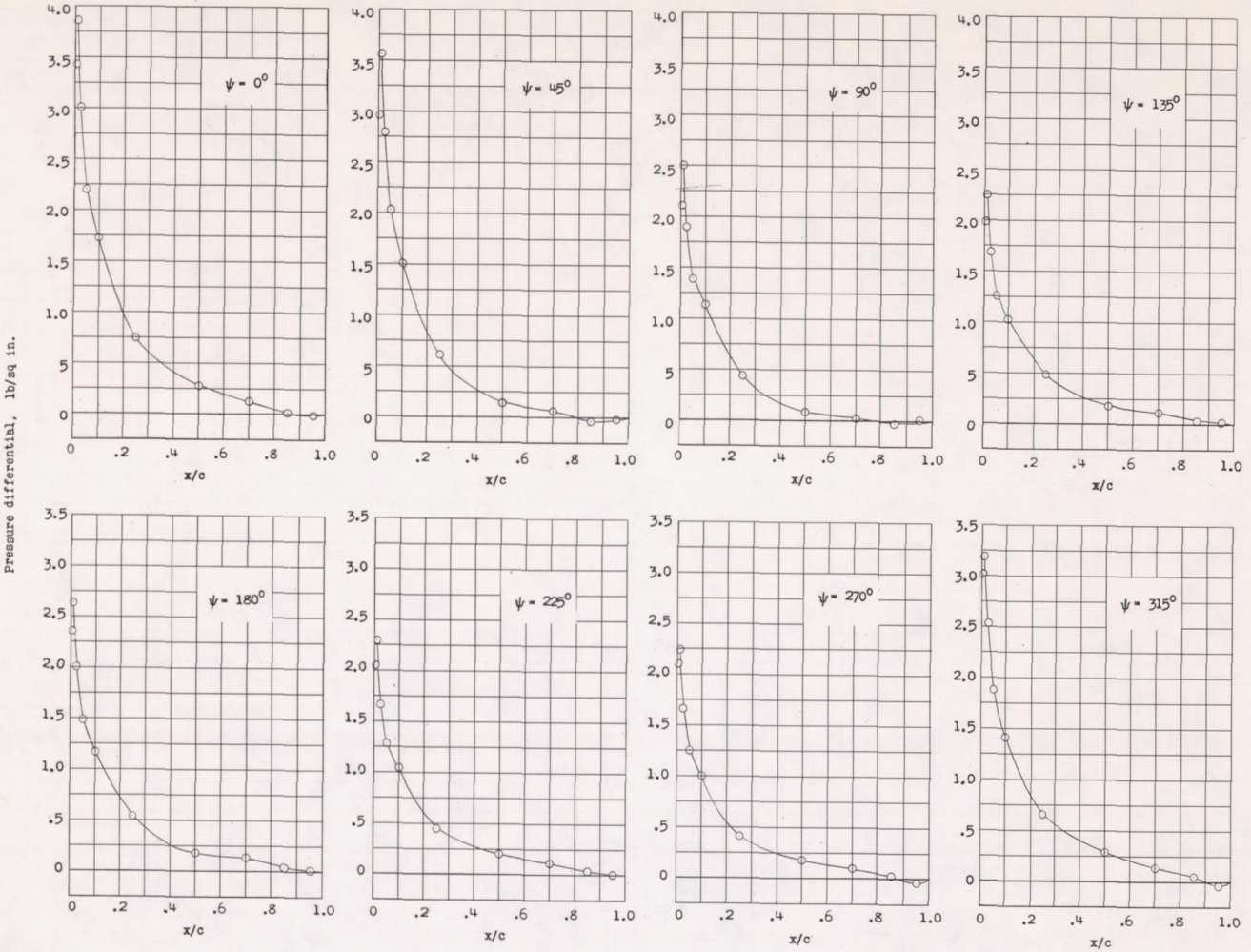

(d) r/R = 0.85.

Figure 5.- Continued.

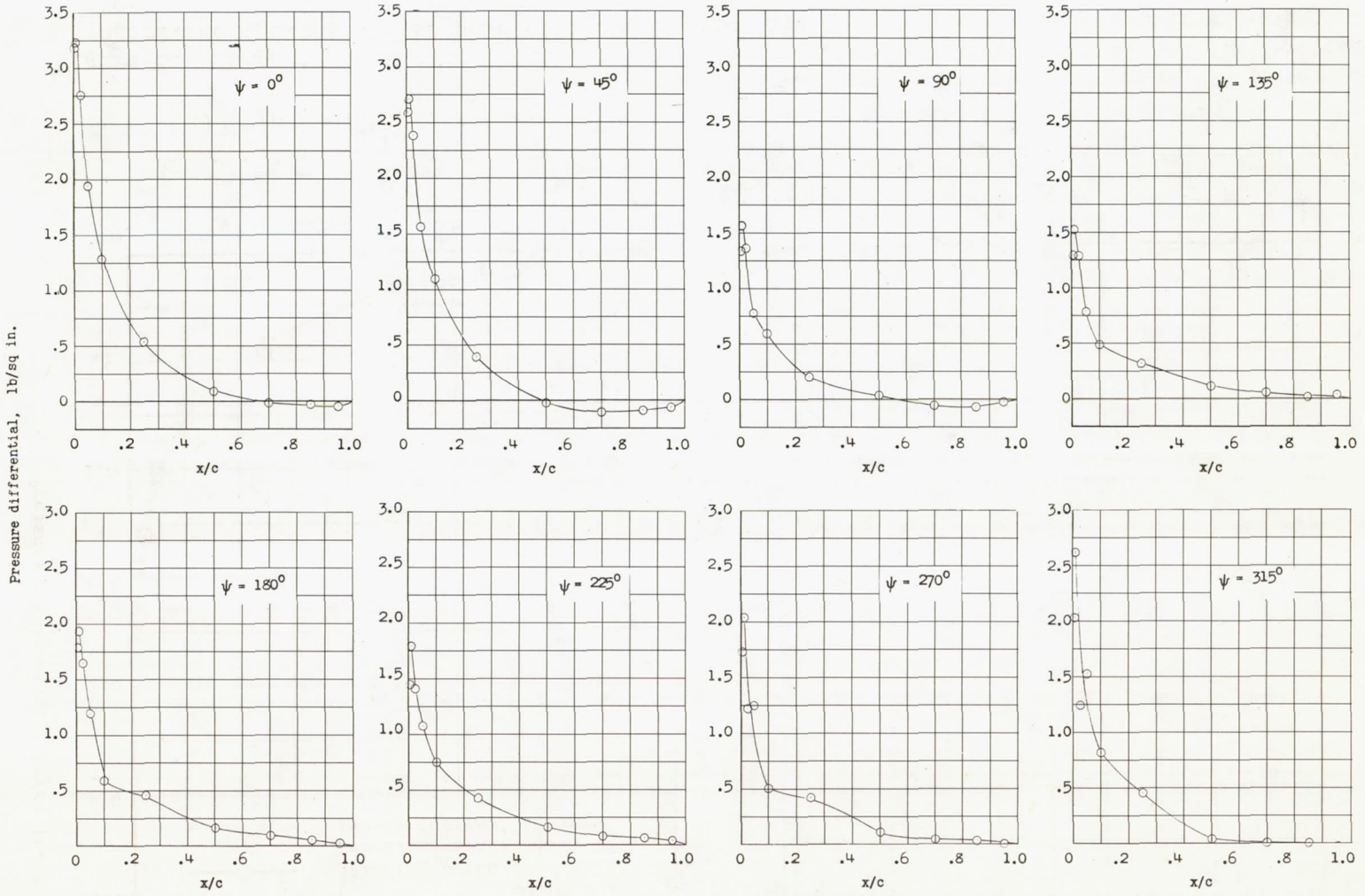

(e) r/R = 0.95.

Figure 5.- Concluded.

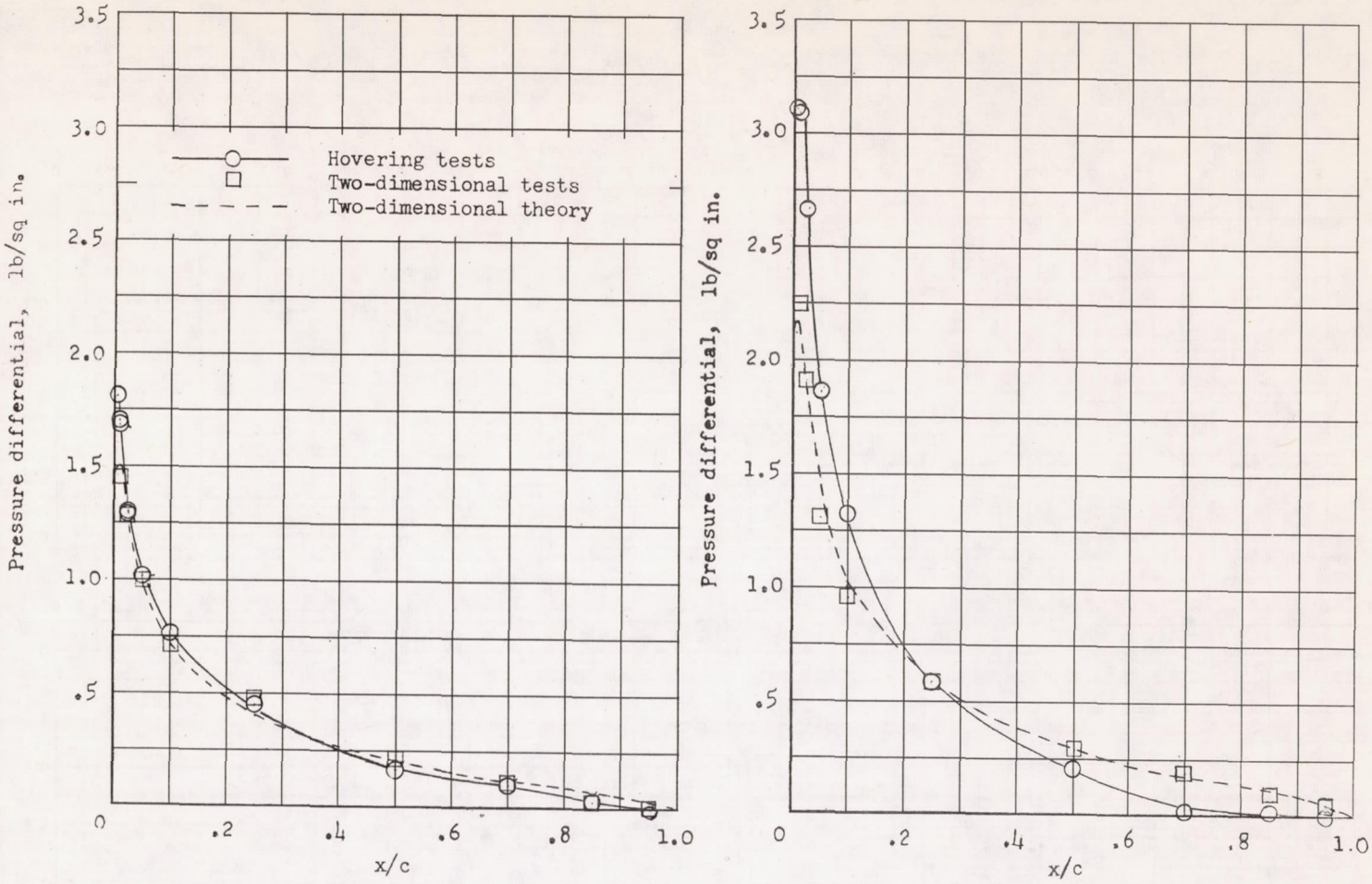

(a) r/R = 0.75; c_l = 0.29.

(b) r/R = 0.95; c_l = 0.26.

Figure 6.- Comparison of experimental hovering tests, two-dimensional tests, and theoretical chordwise loading at the same lift coefficient for two radial locations. For hovering tests, ΩR = 496 ft/sec; θ = 8.5°.

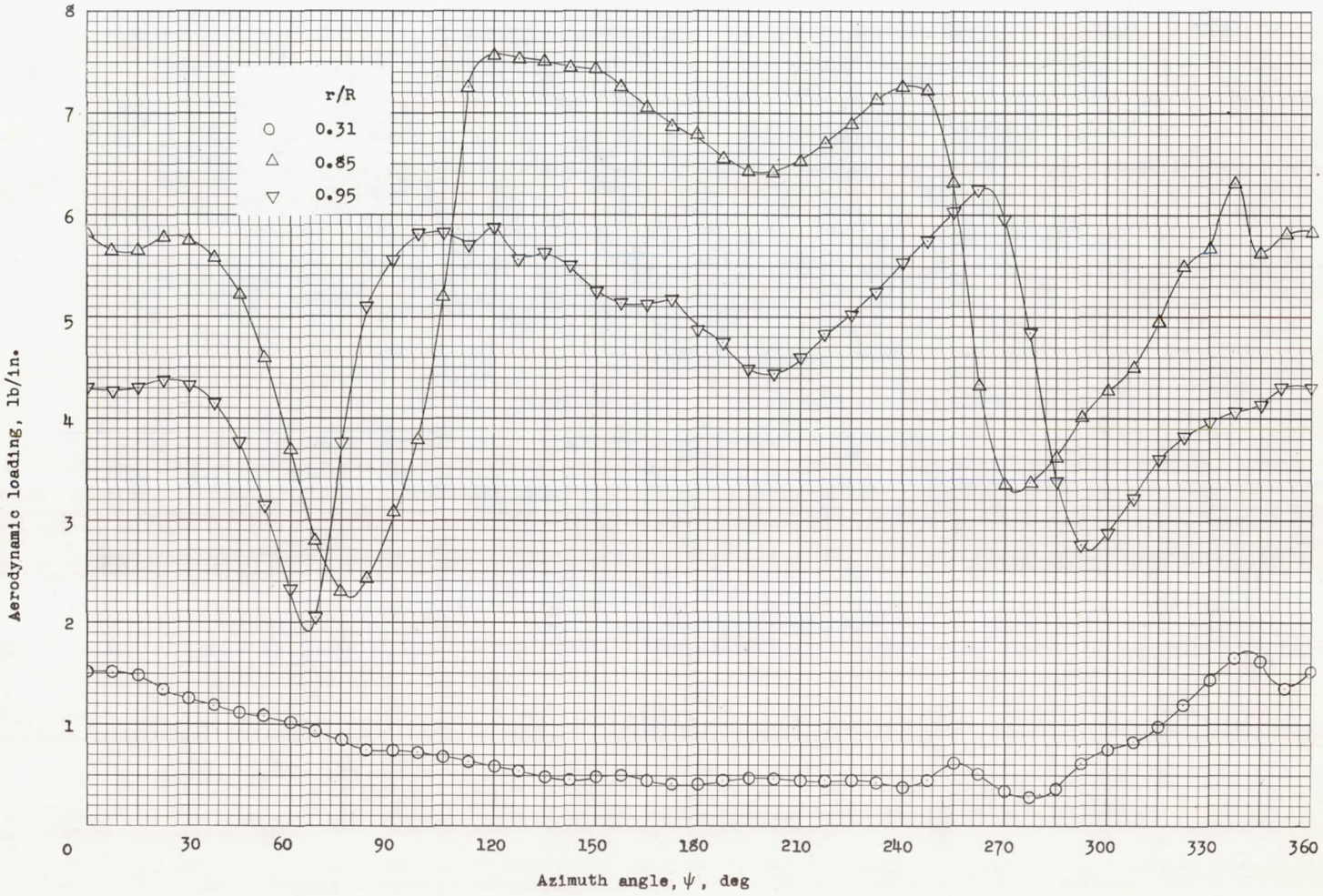

(a) $\mu = 0.08$.

Figure 7.- Variation of section aerodynamic loading with azimuth at various spanwise stations.

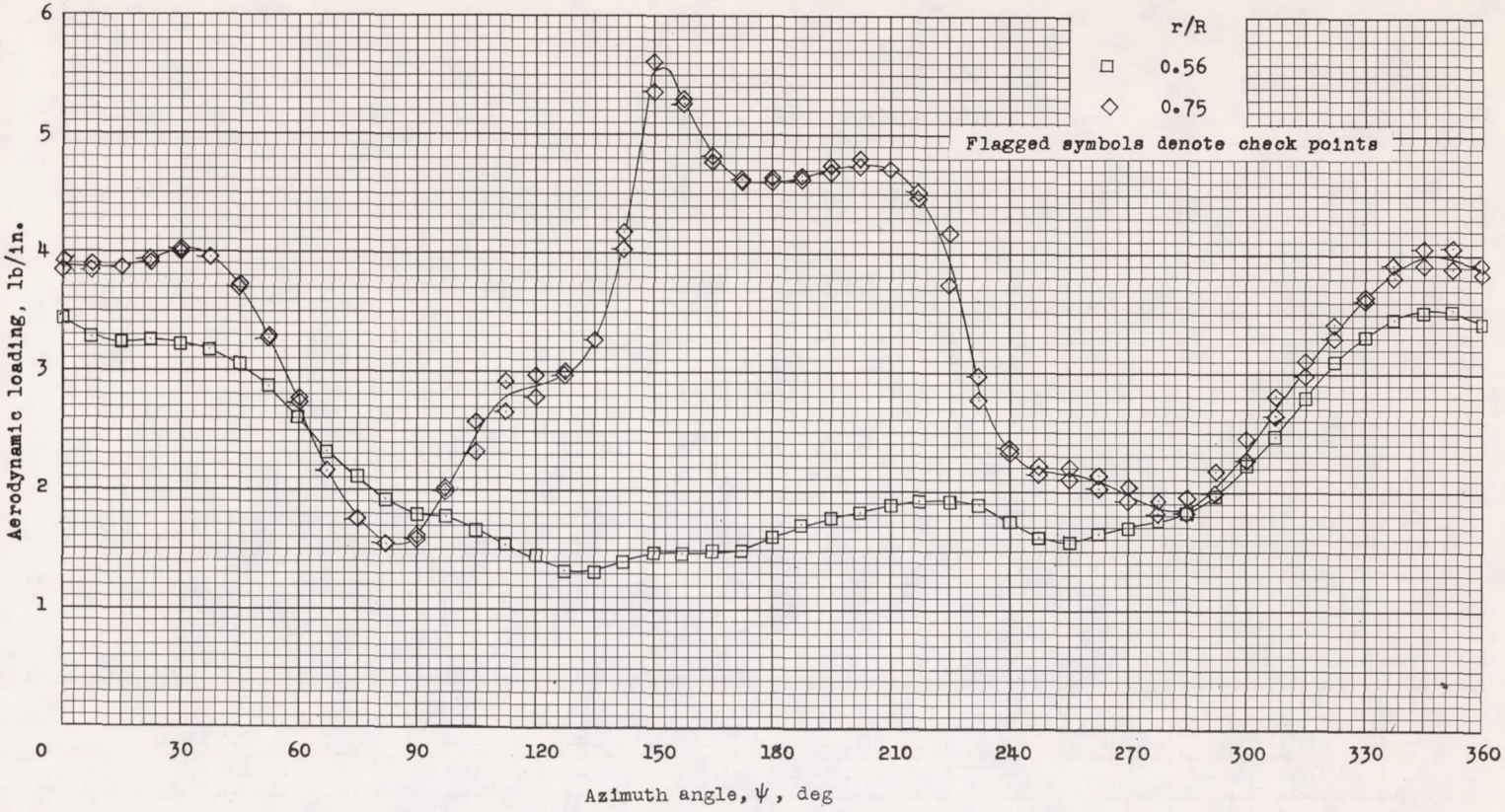

(a) Concluded.

Figure 7.- Continued.

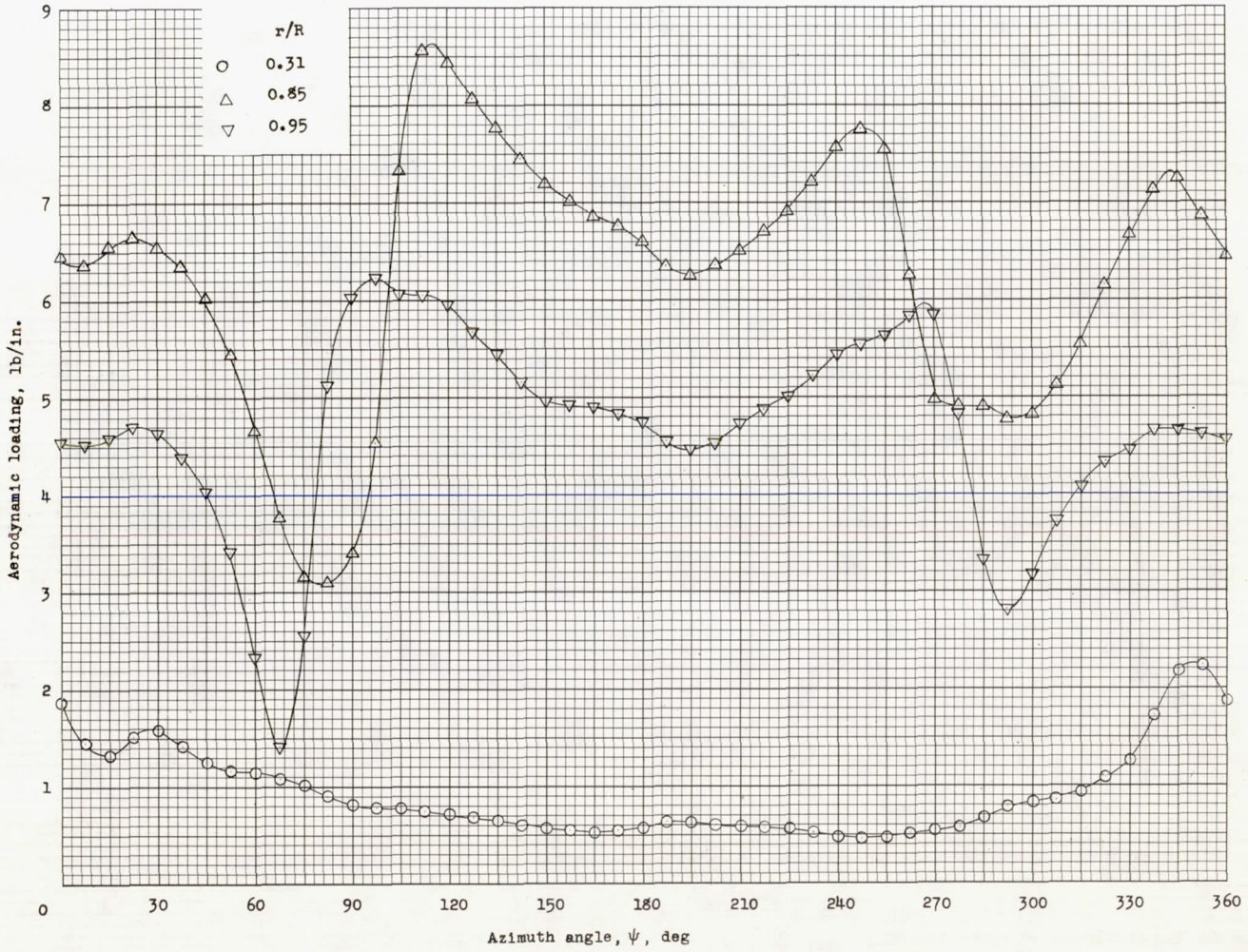

(b) $\mu = 0.10$.

Figure 7.- Continued.

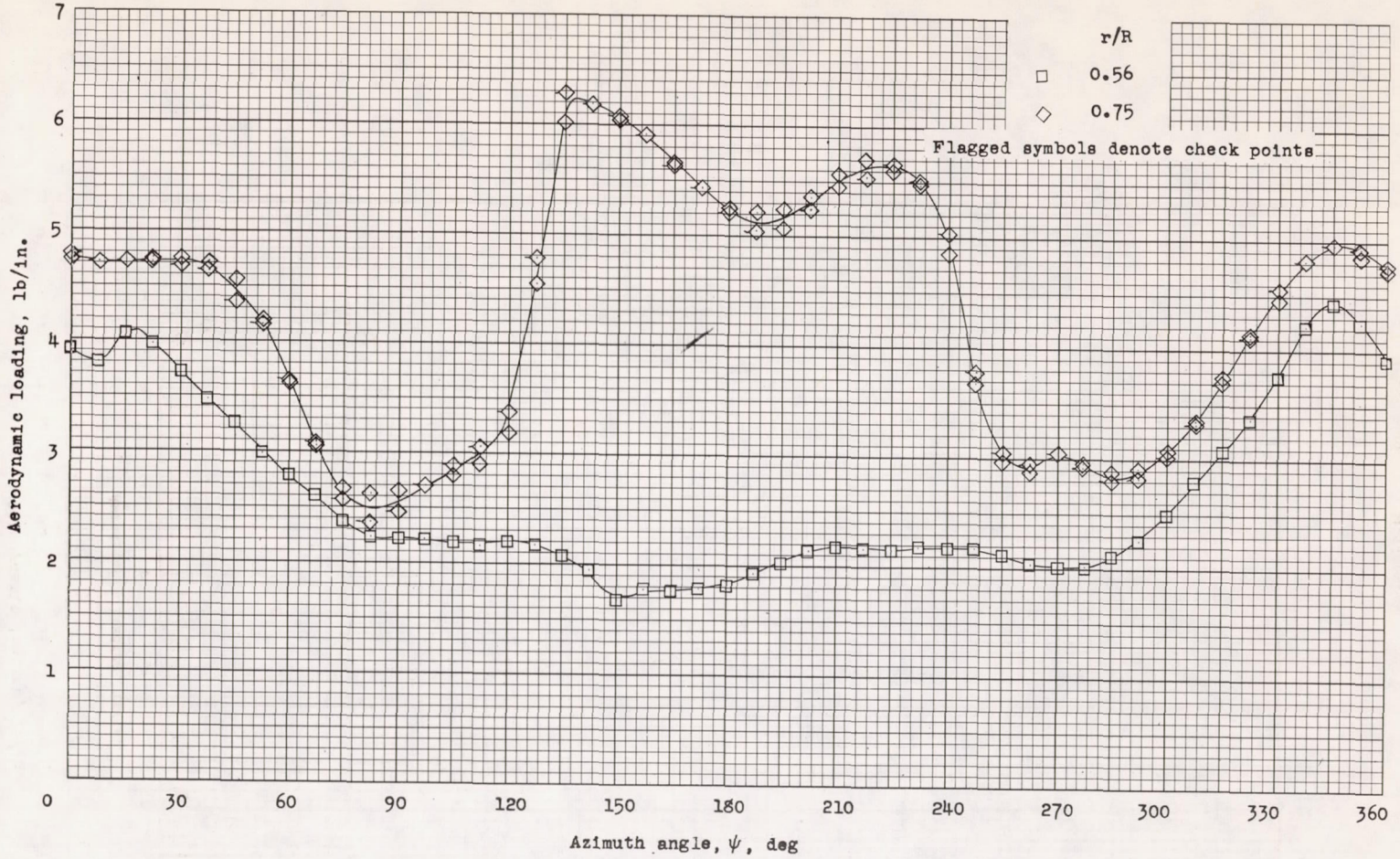

(b) Concluded.

Figure 7.- Continued.

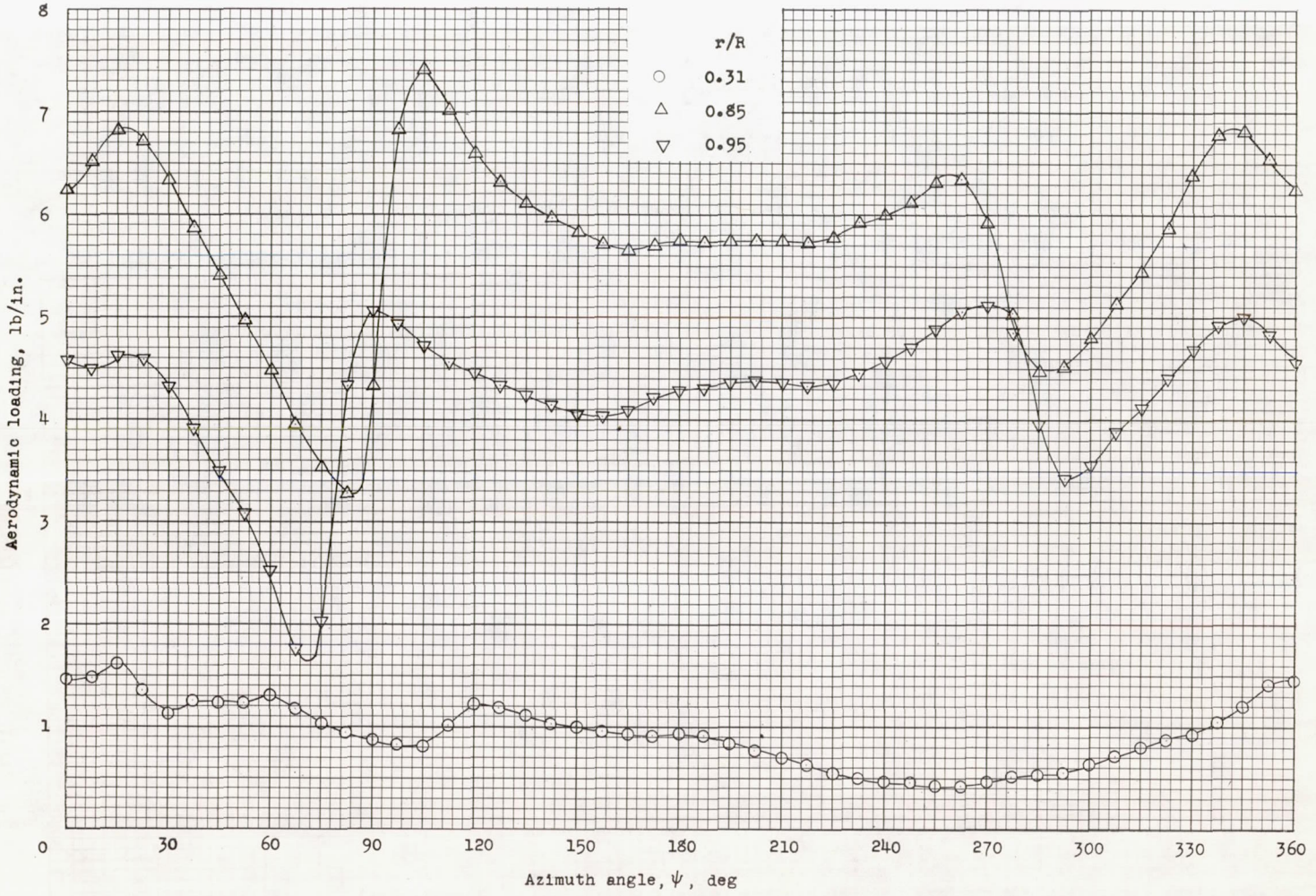

(c) $\mu = 0.15$.

Figure 7.- Continued.

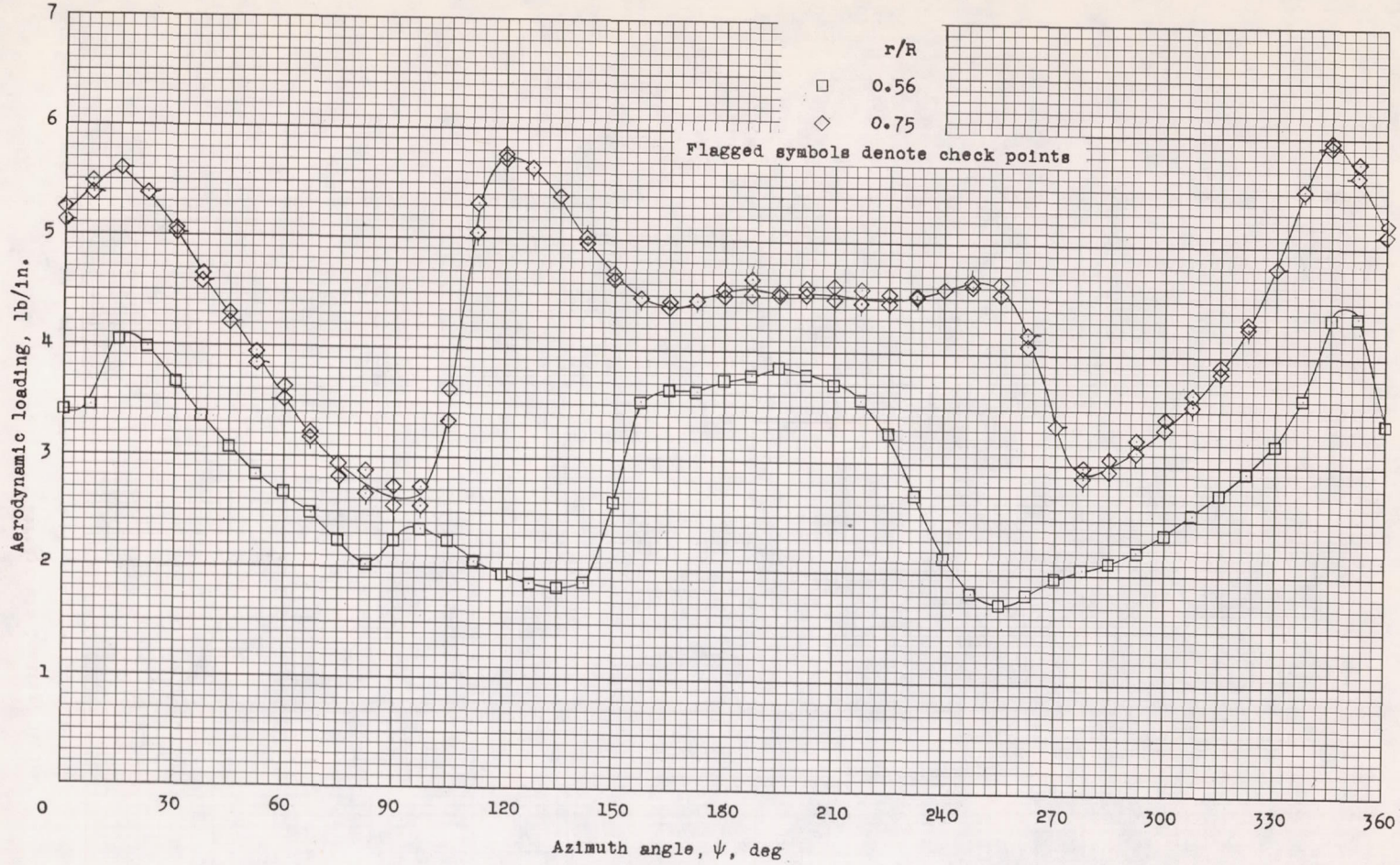

(c) Concluded.

Figure 7.- Continued.

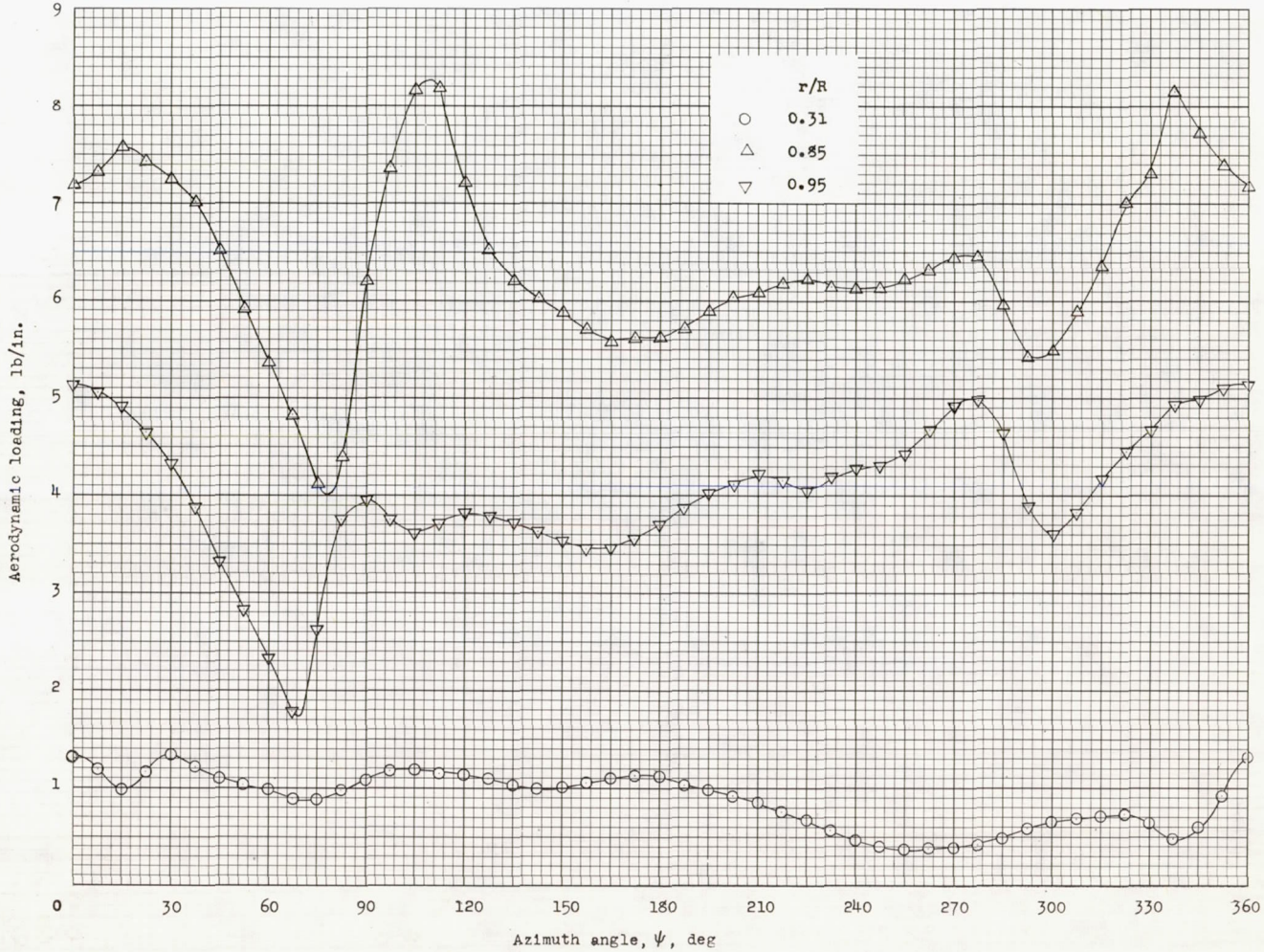

(d) $\mu = 0.20$.

Figure 7.- Continued.

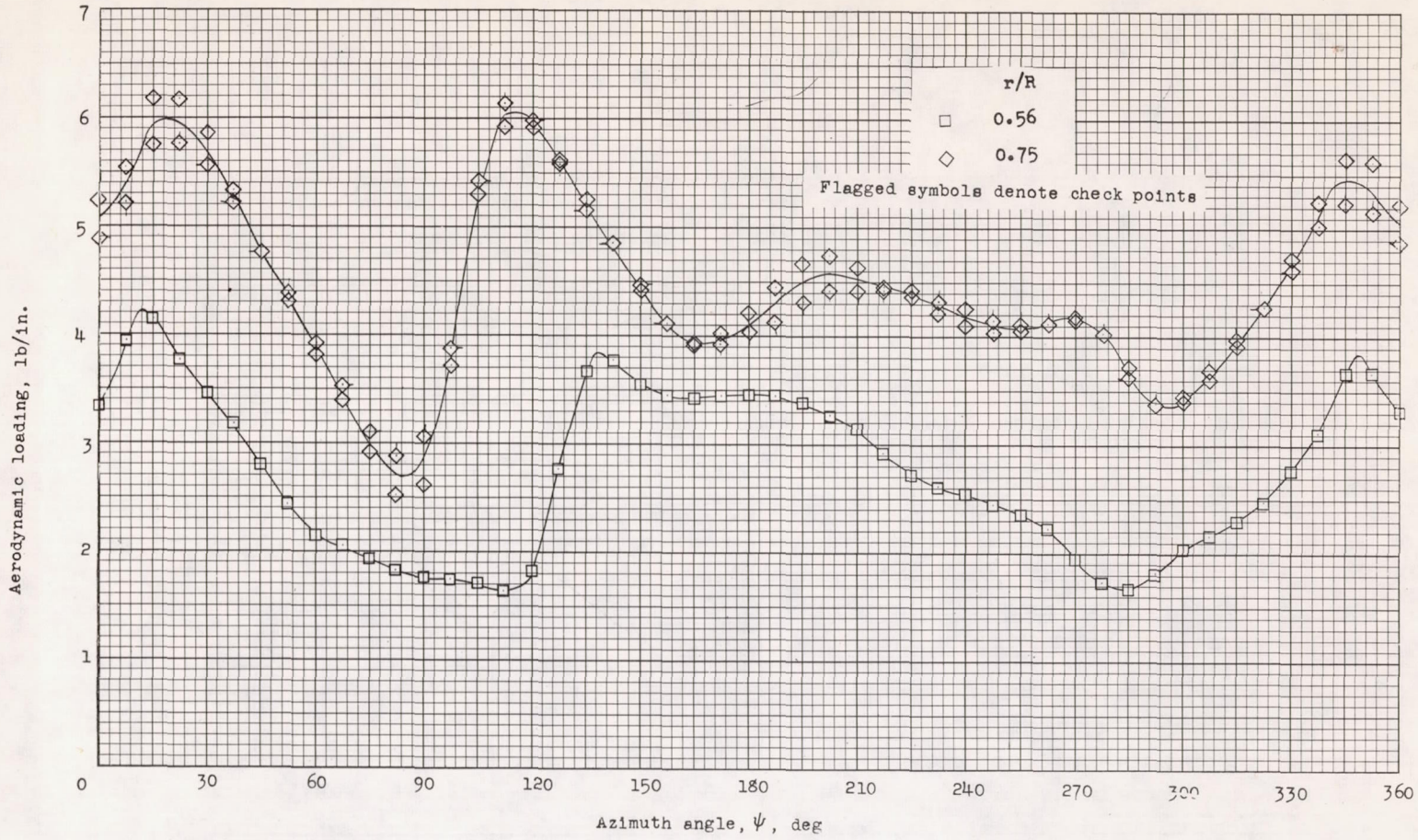

(d) Concluded.

Figure 7.- Continued.

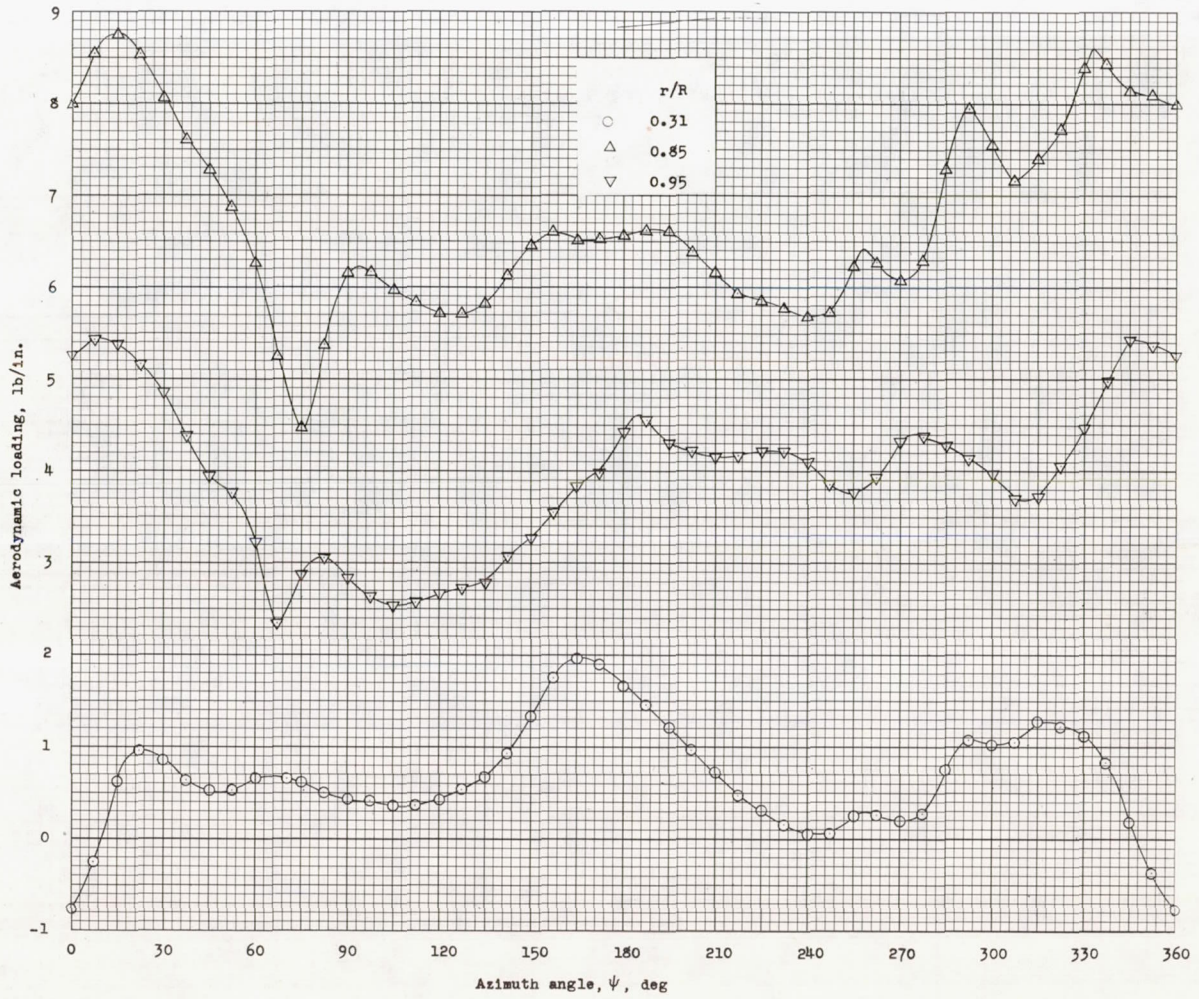

(e) $\mu = 0.24$.

Figure 7.- Continued.

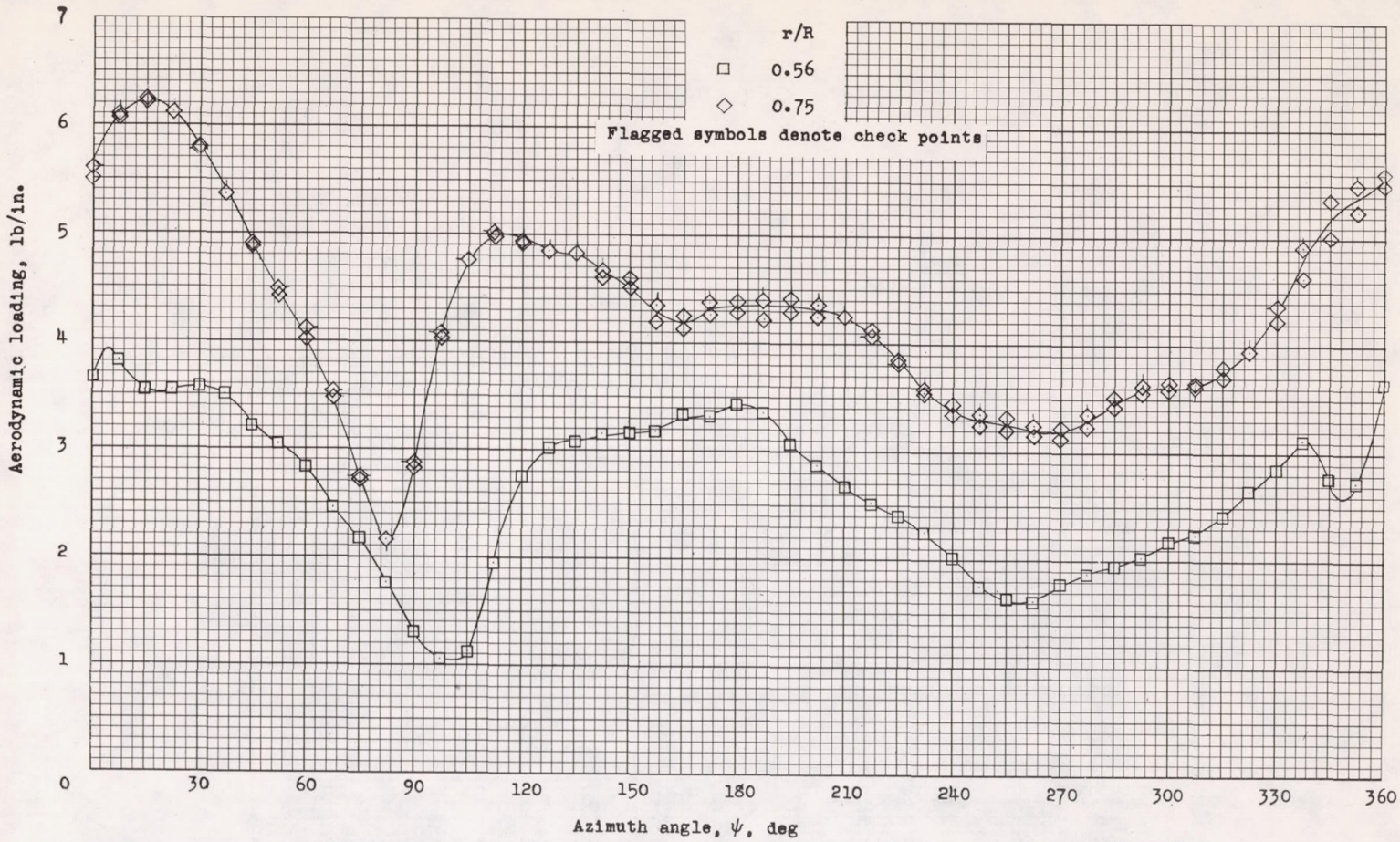

(e) Concluded.

Figure 7.- Continued.

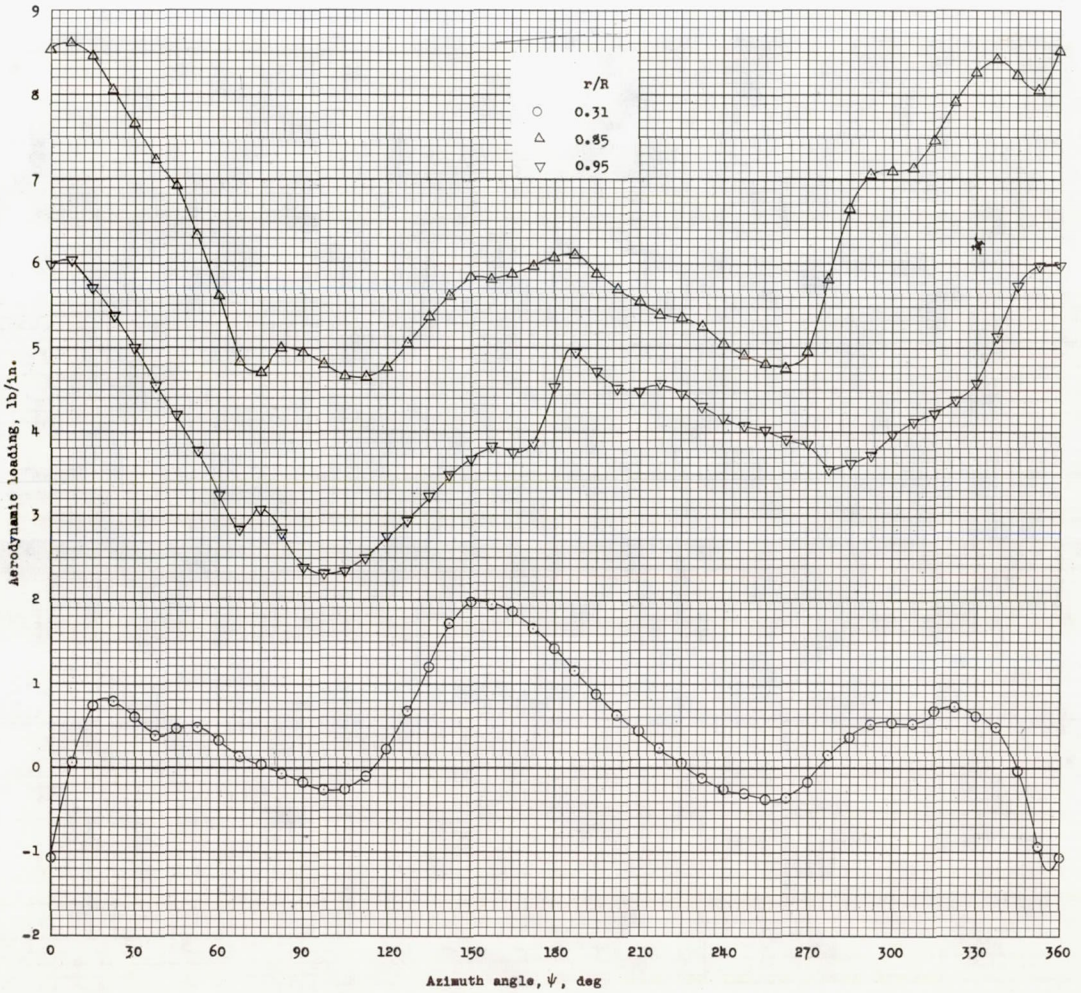

(f) $\mu = 0.29$.

Figure 7.- Continued.

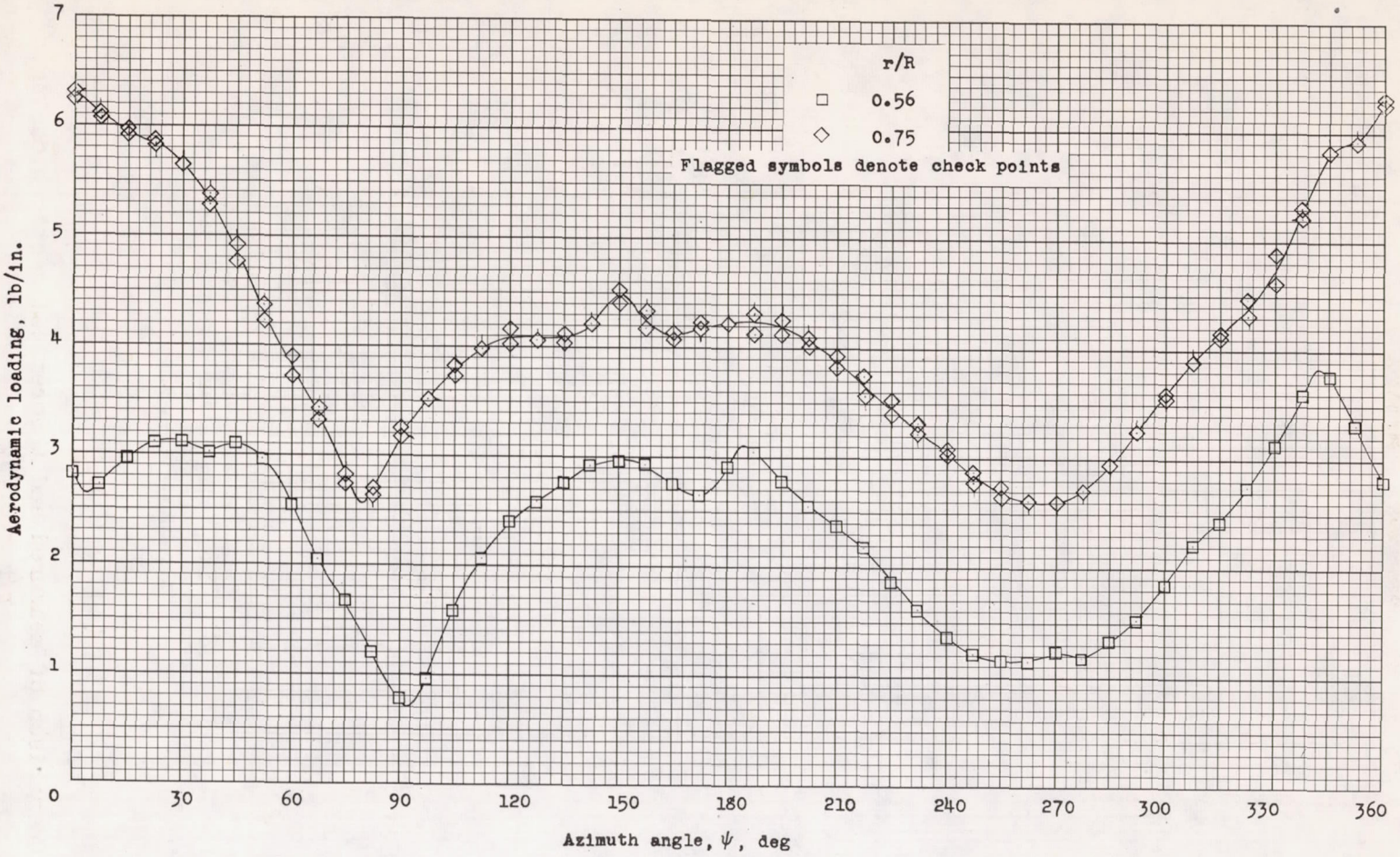

(f) Concluded.

Figure 7.- Concluded.

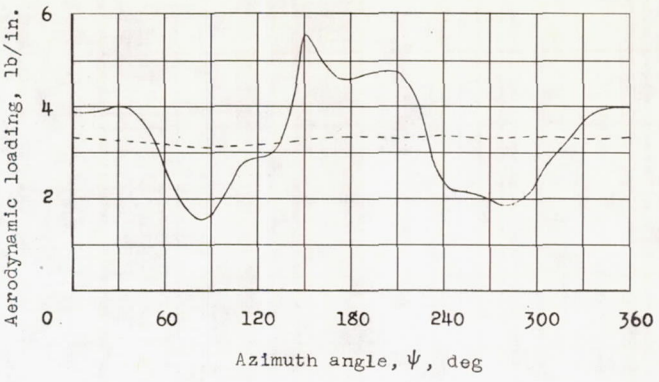

(a) $\mu = 0.08$.

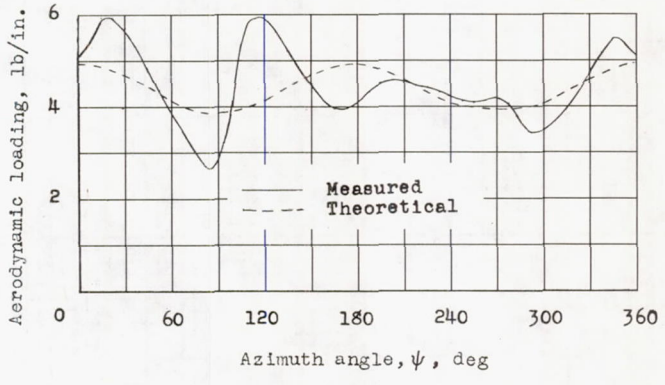

(b) $\mu = 0.20$.

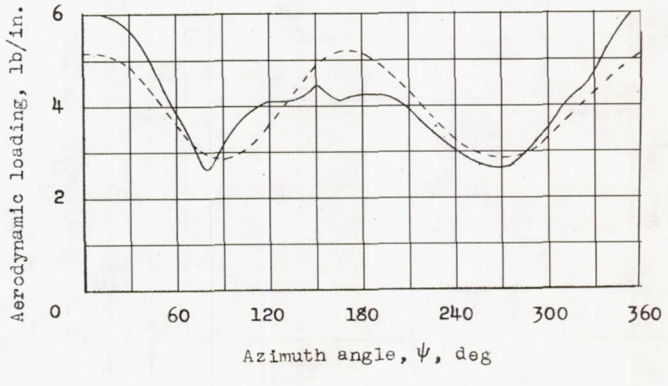

(c) $\mu = 0.29$.

Figure 8.- Comparison of measured and theoretical section loading. $r/R = 0.75$.

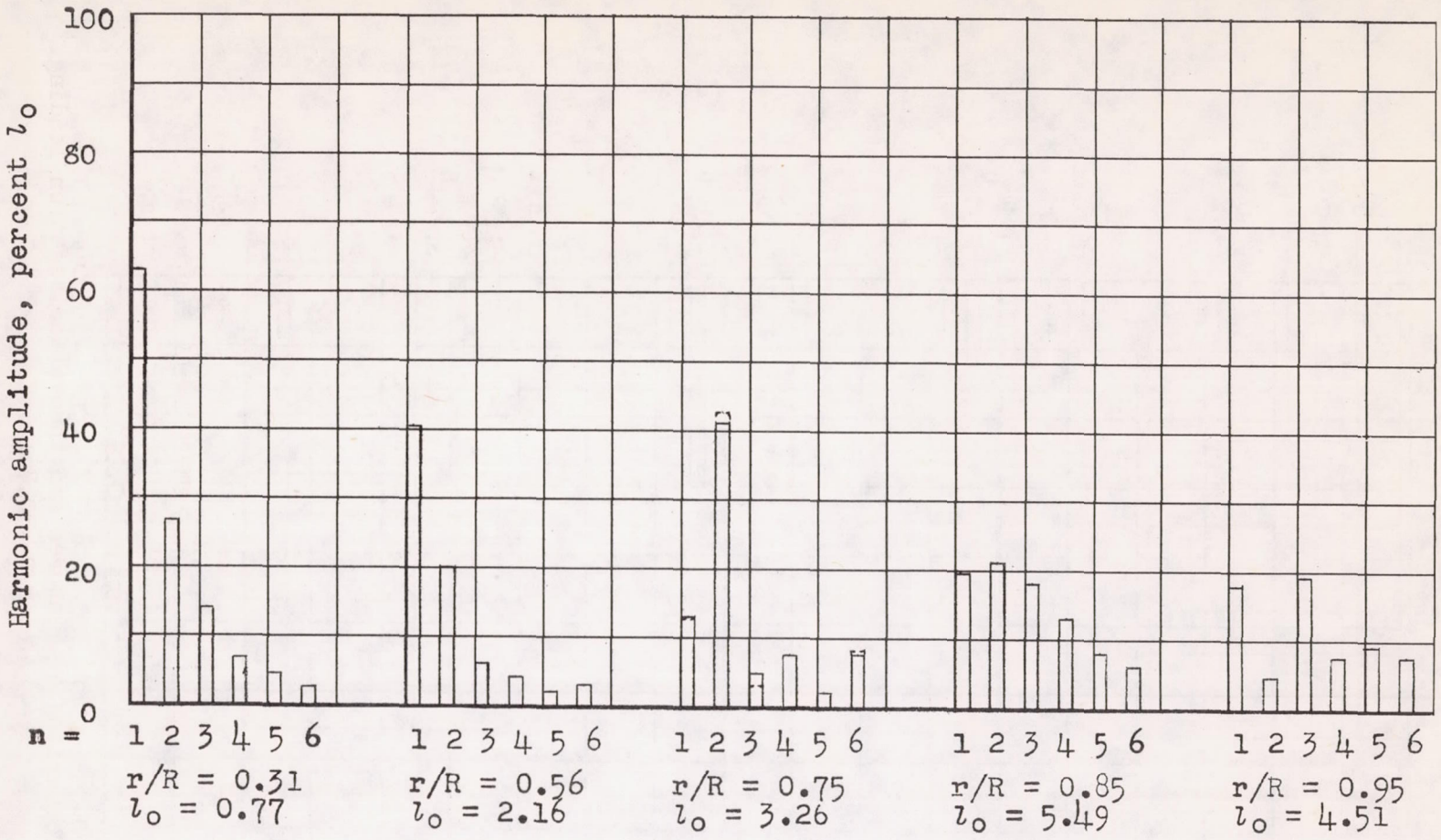

(a) $\mu = 0.08$.

Figure 9.- Harmonic amplitude of section aerodynamic loading as percent of steady section load.

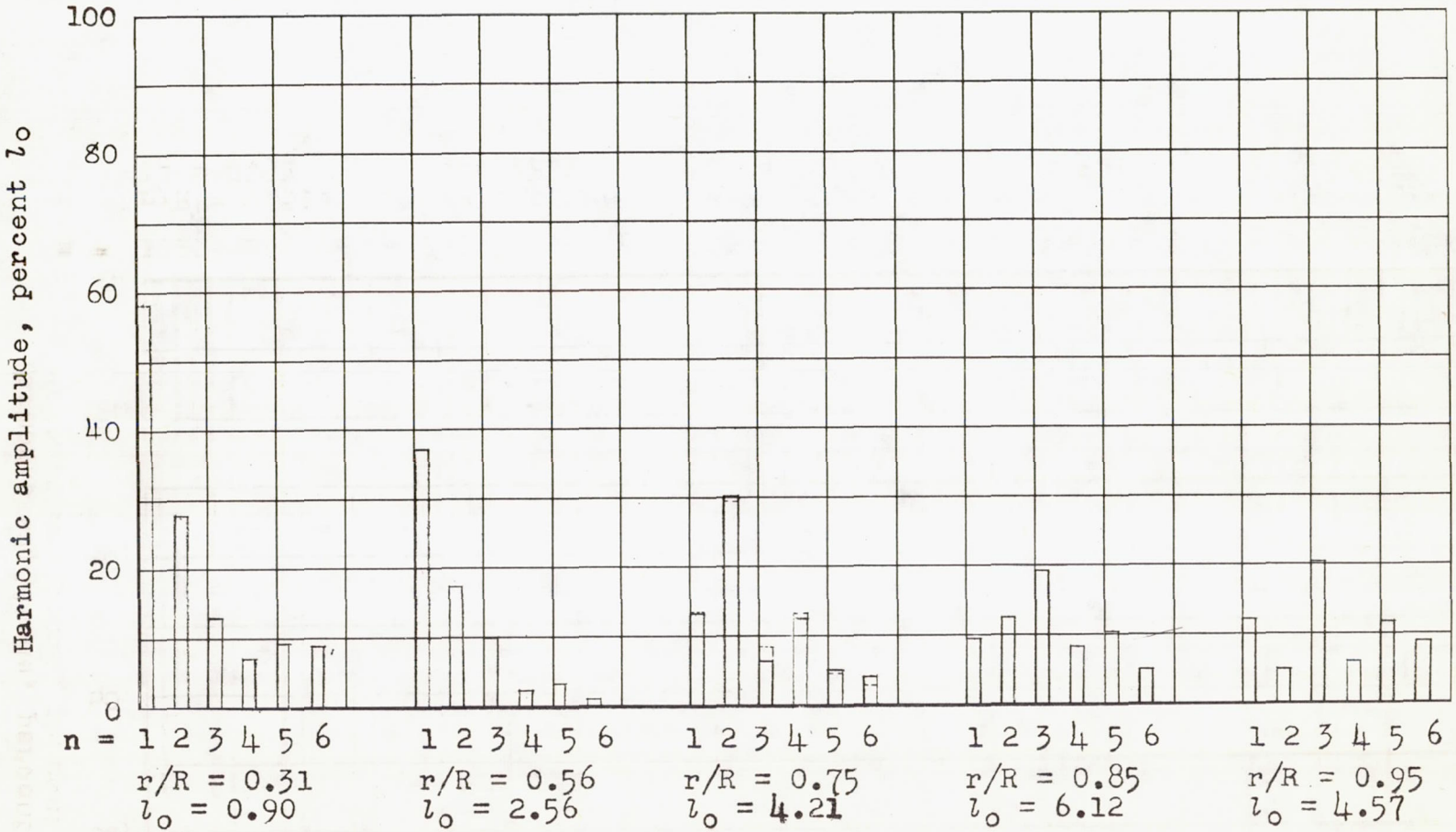

(b) $\mu = 0.10$.

Figure 9.- Continued.

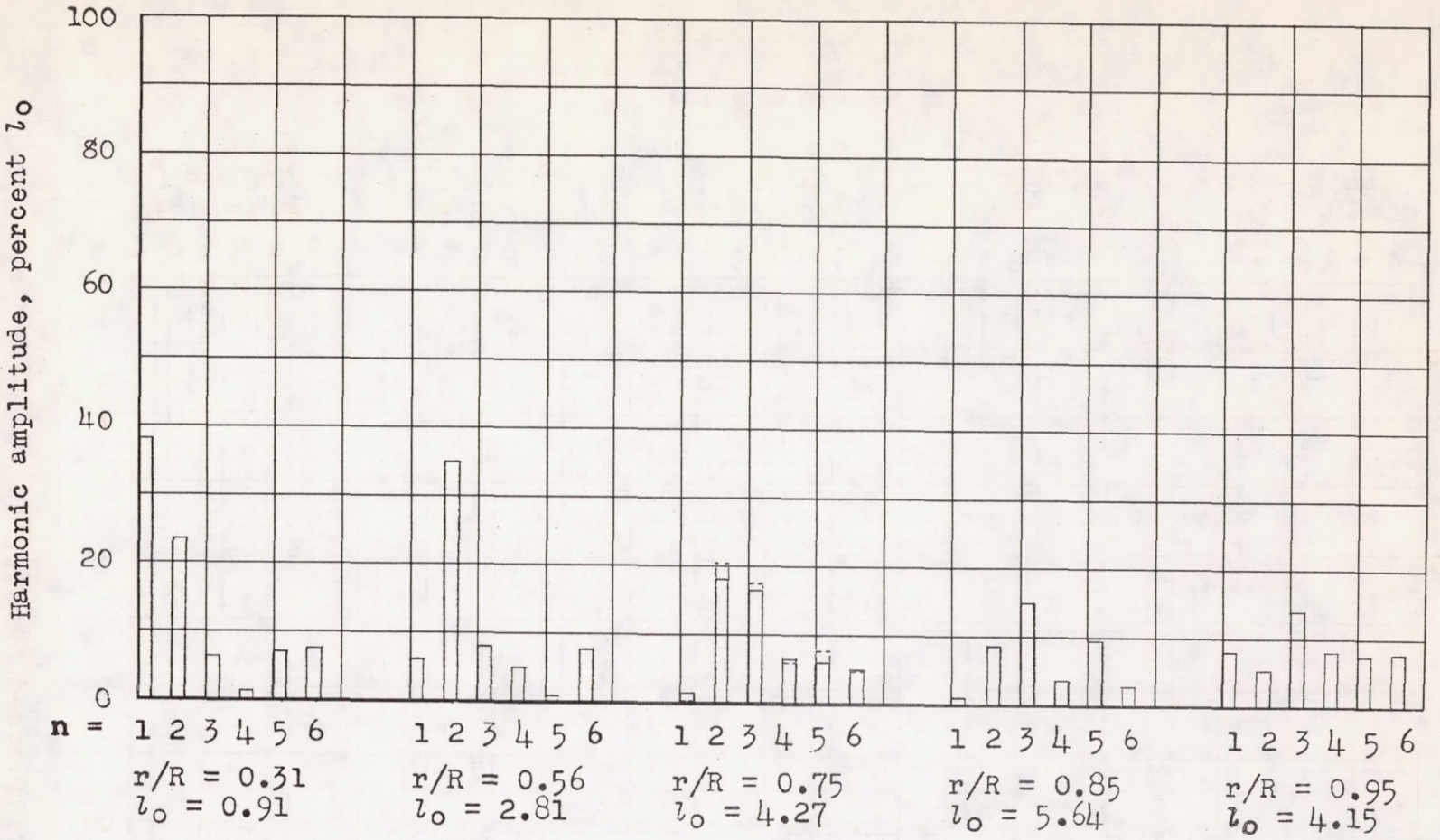

(c) $\mu = 0.15$.

Figure 9.- Continued.

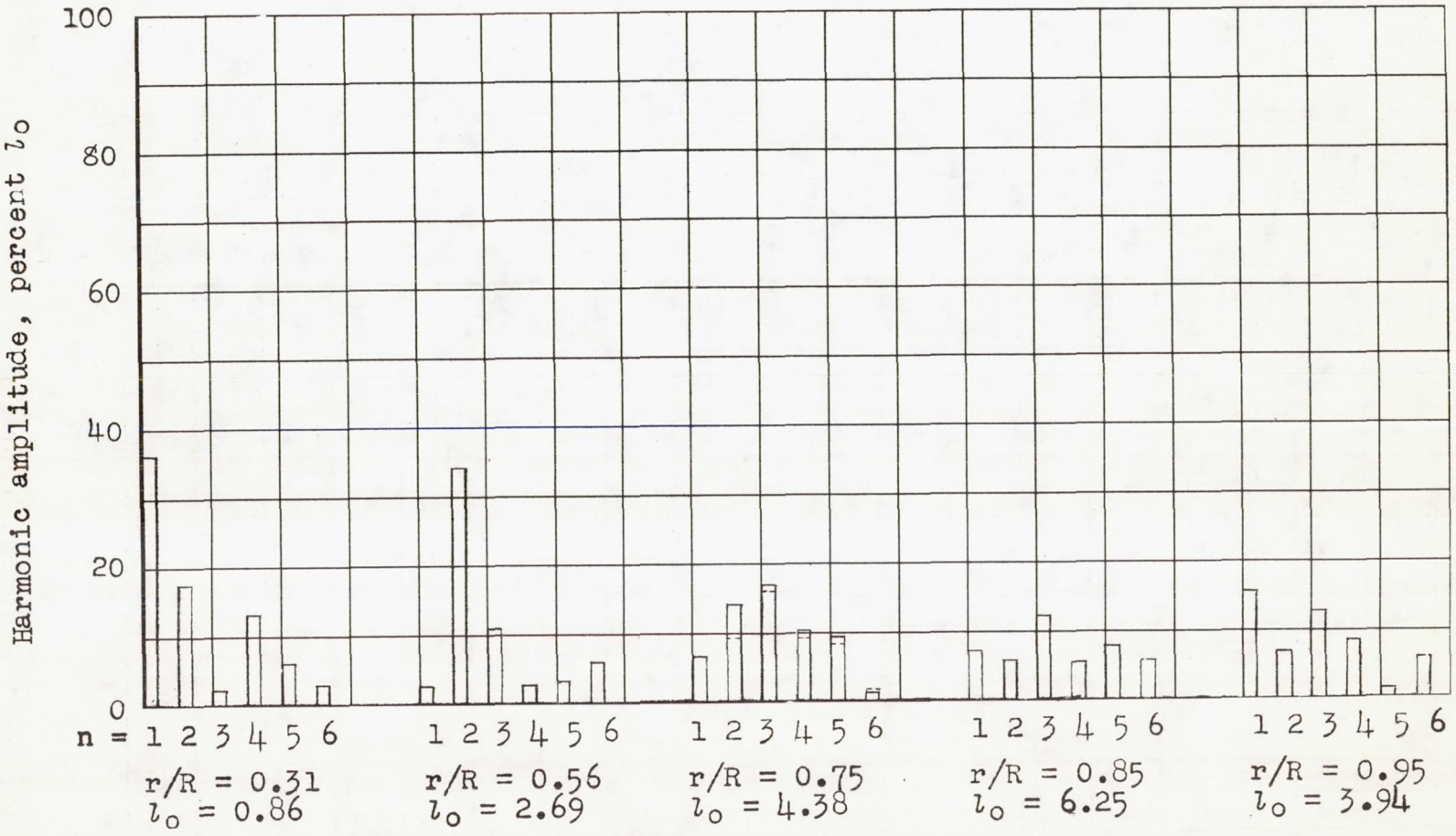

(d) $\mu = 0.20$.

Figure 9.- Continued.

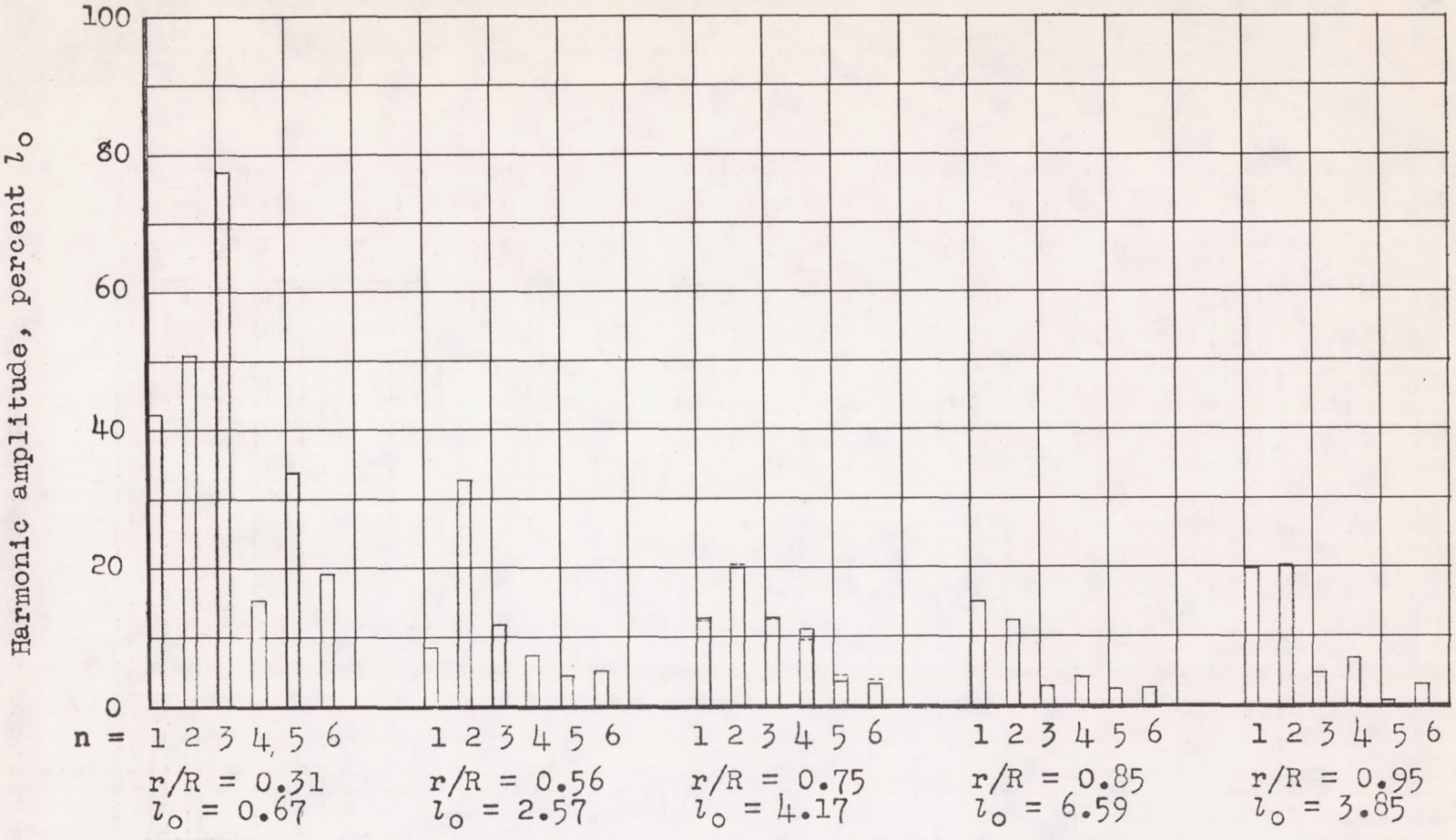

(e) $\mu = 0.24$.

Figure 9.- Continued.

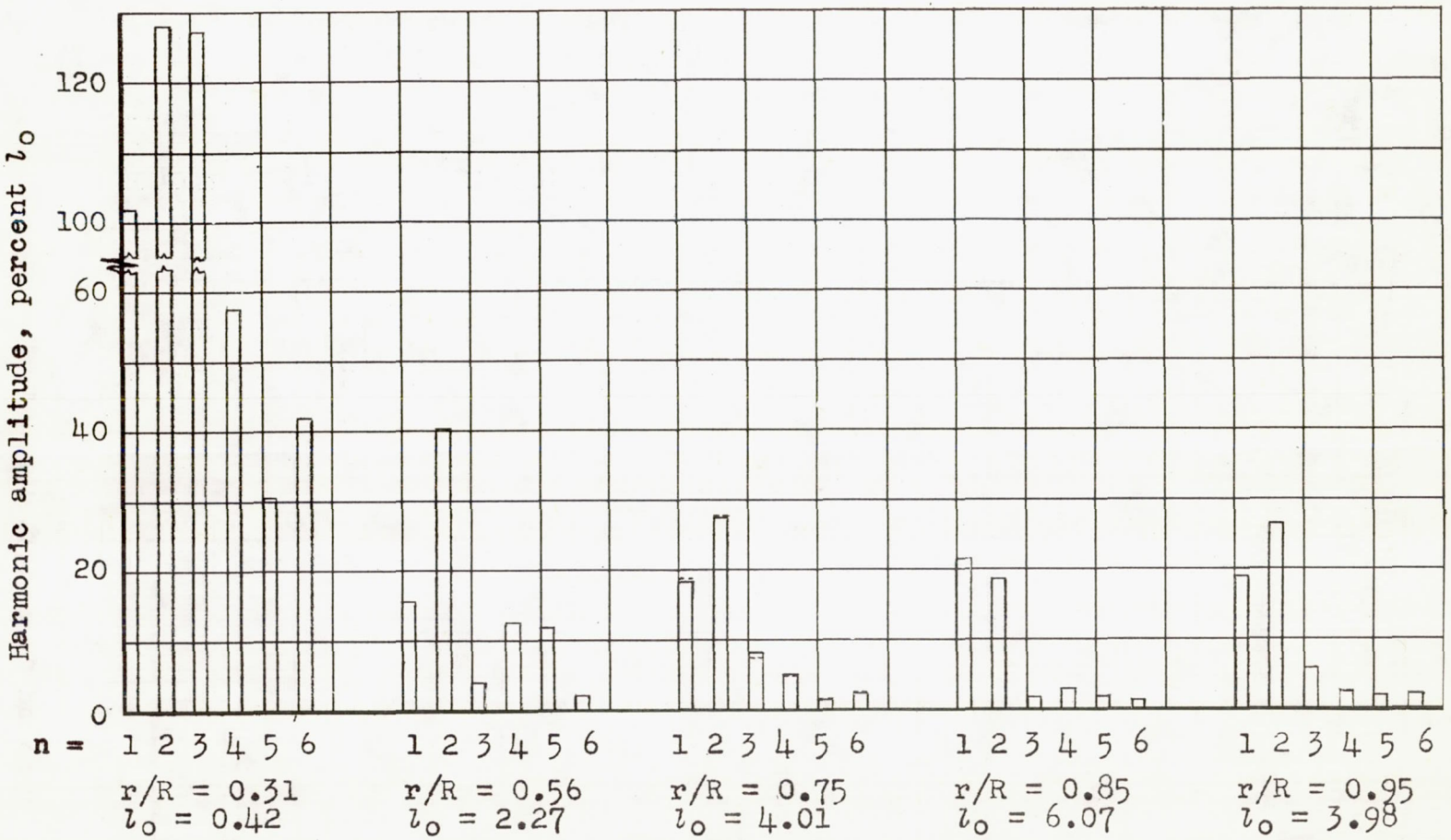

(f) $\mu = 0.29$.

Figure 9.- Concluded.

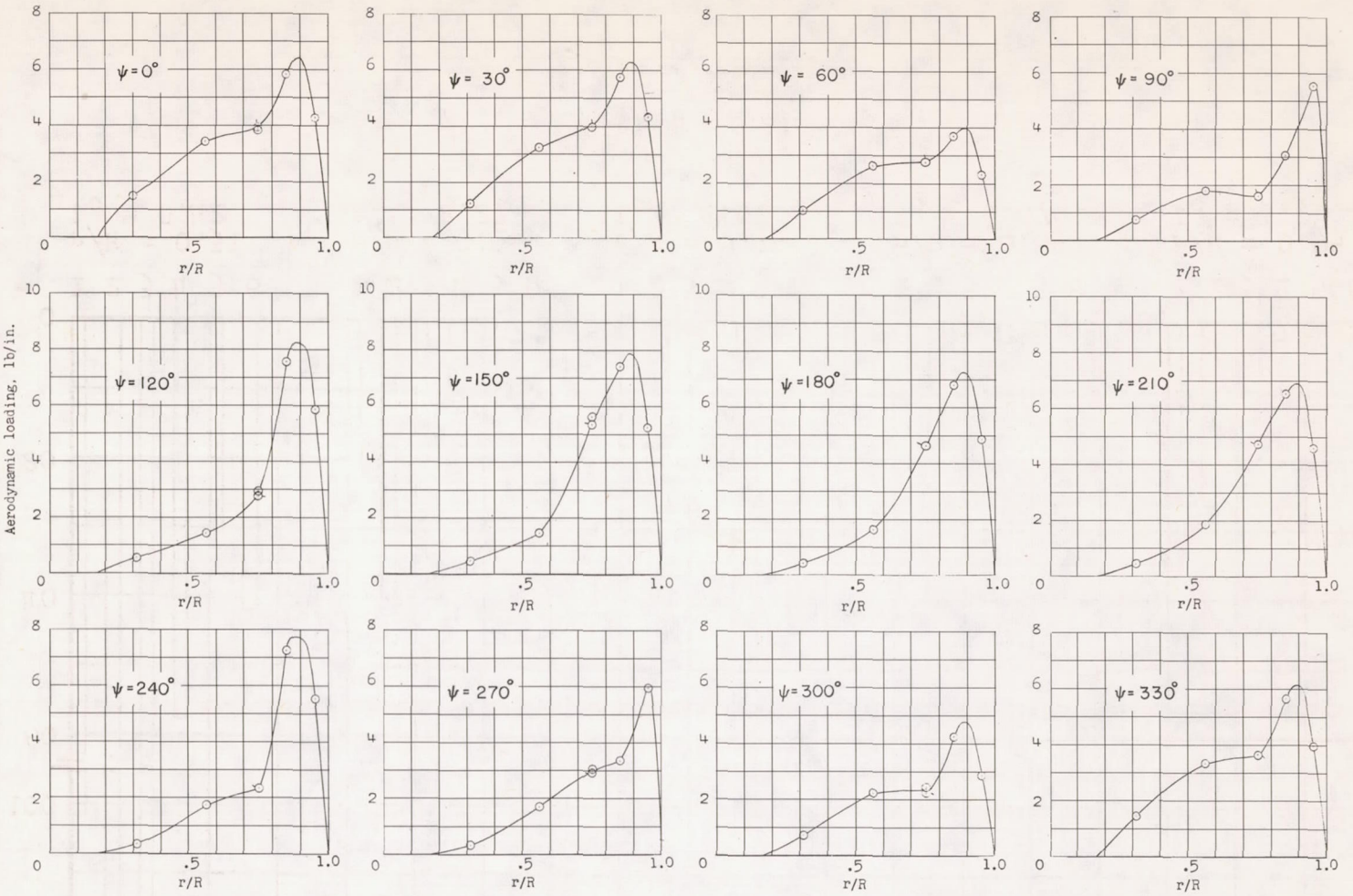

(a) $\mu = 0.08$.

Figure 10.- Spanwise aerodynamic load distribution at various azimuth positions.

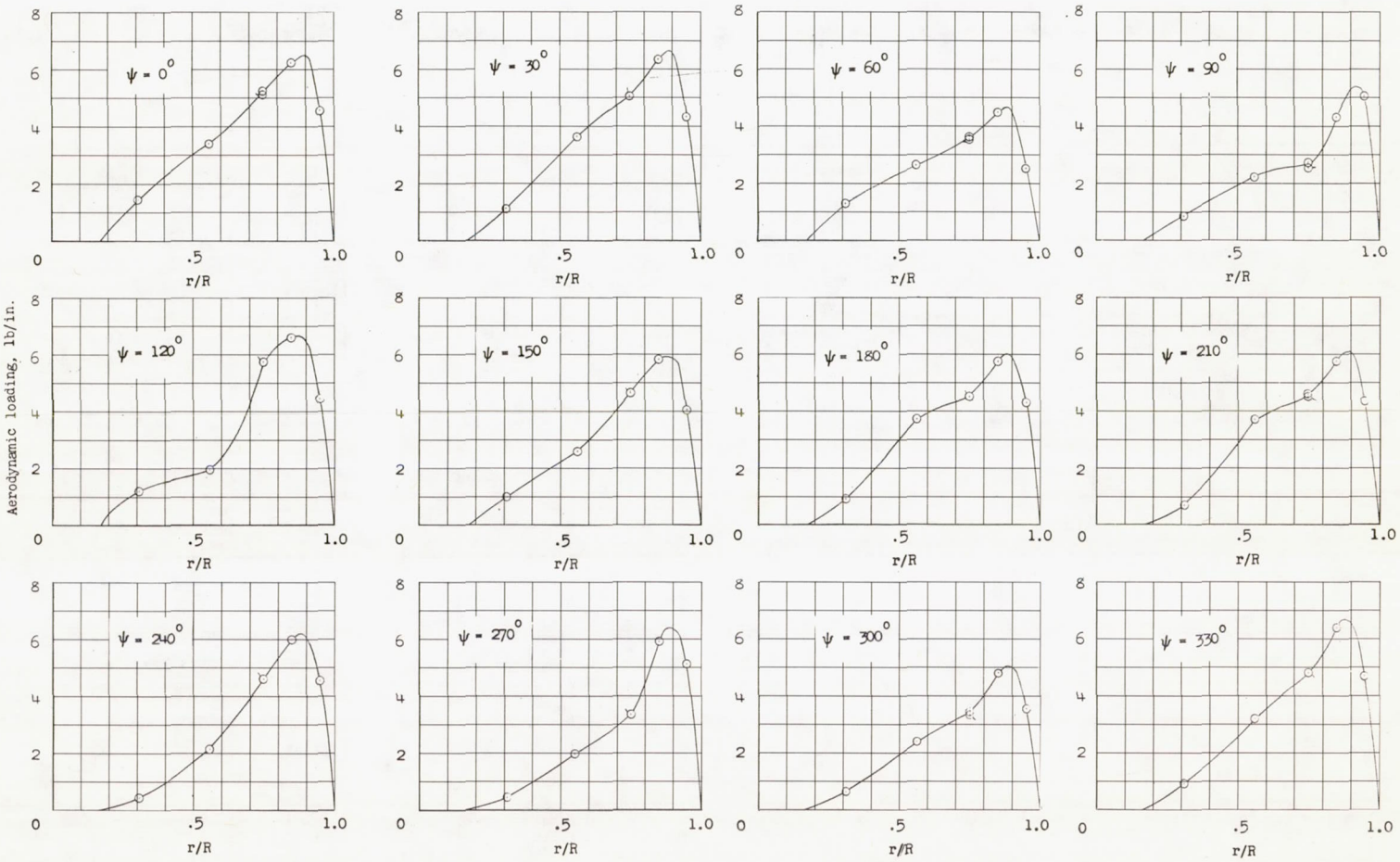

(b) $\mu = 0.15$.

Figure 10.- Continued.

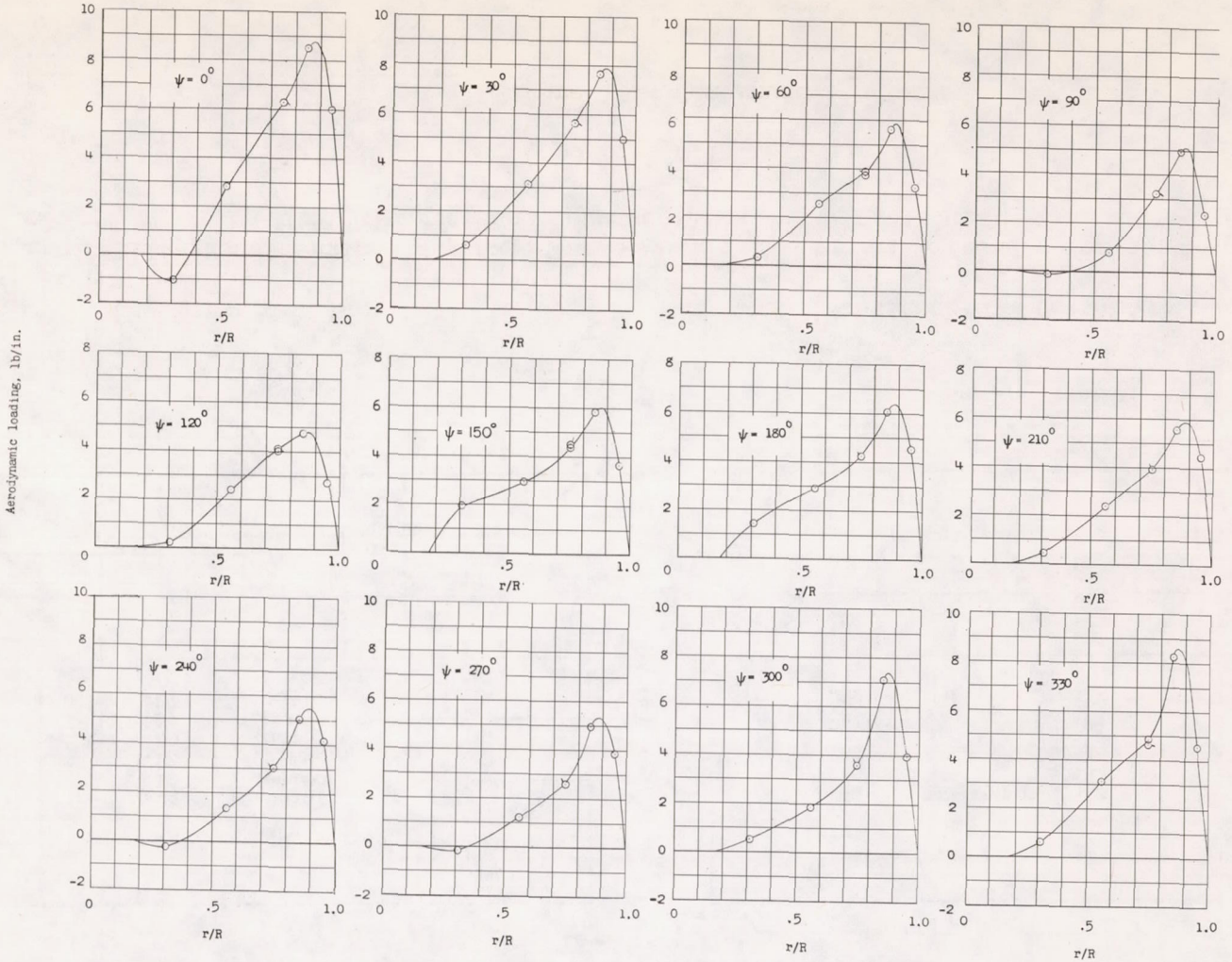

(c) $\mu = 0.29$.

Figure 10.- Concluded.

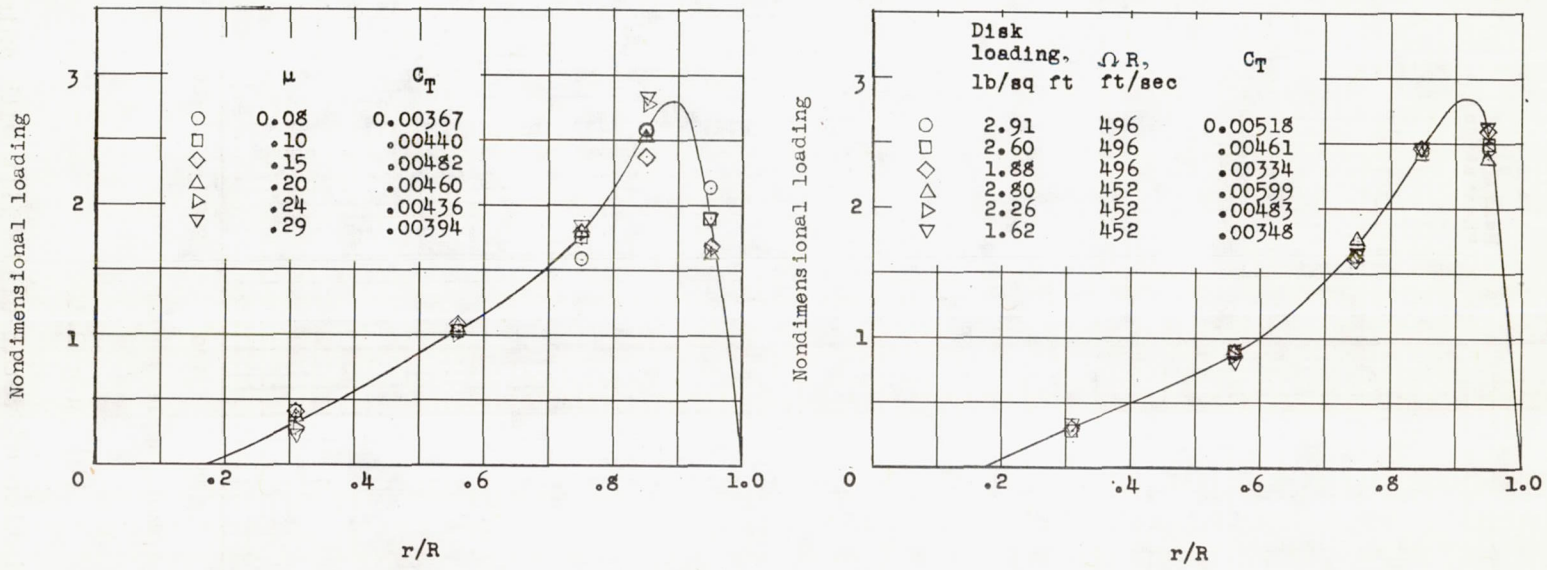

(a) Forward flight.

(b) Static thrust (ref. 6).

Figure 11.- Nondimensional spanwise aerodynamic loading distribution for several static-thrust and forward-flight conditions.

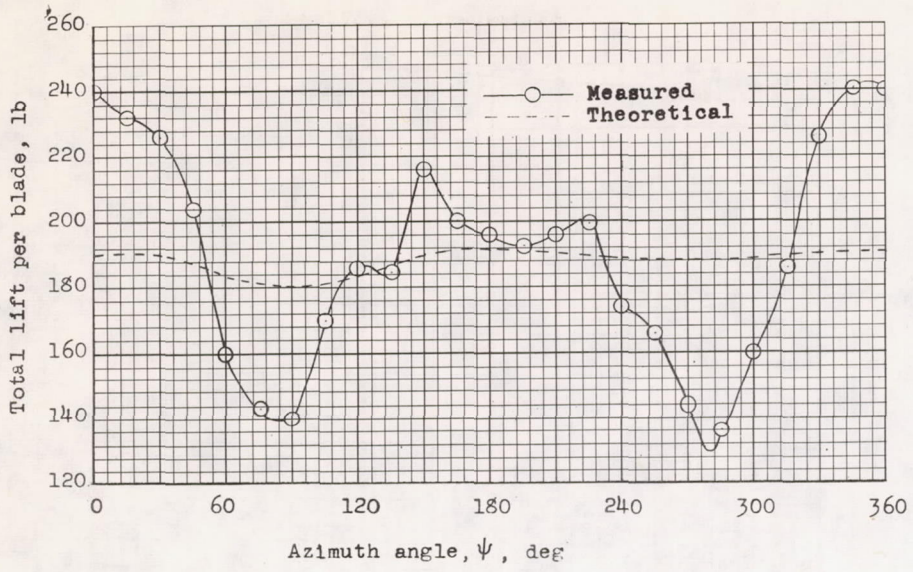

(a) $\mu = 0.08$.

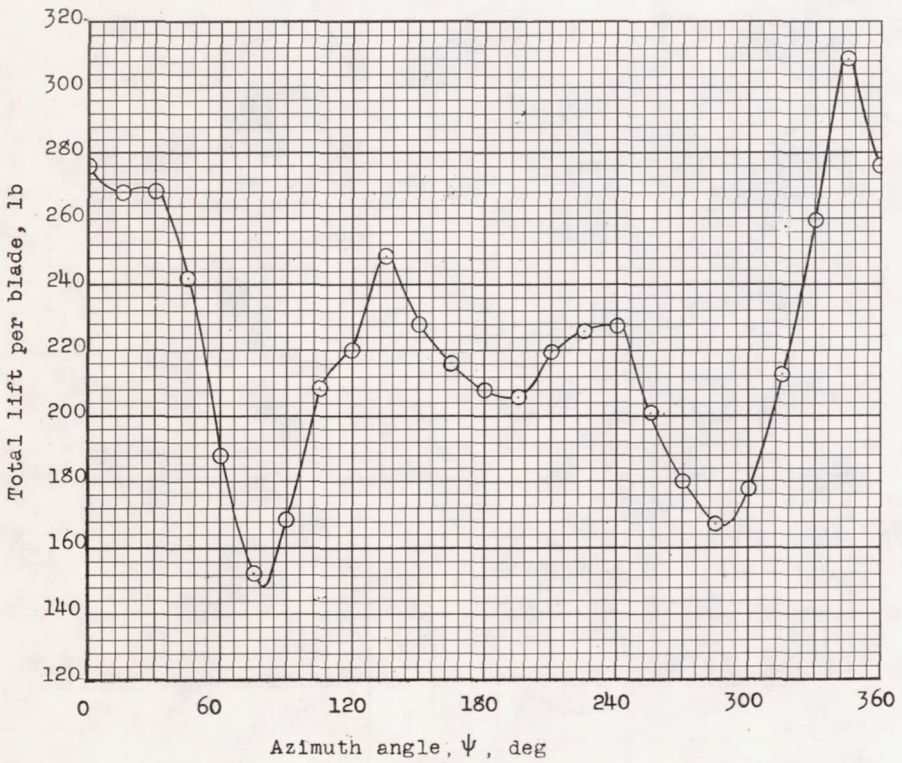

(b) $\mu = 0.10$.

Figure 12.- Variation of total blade lift with azimuth.

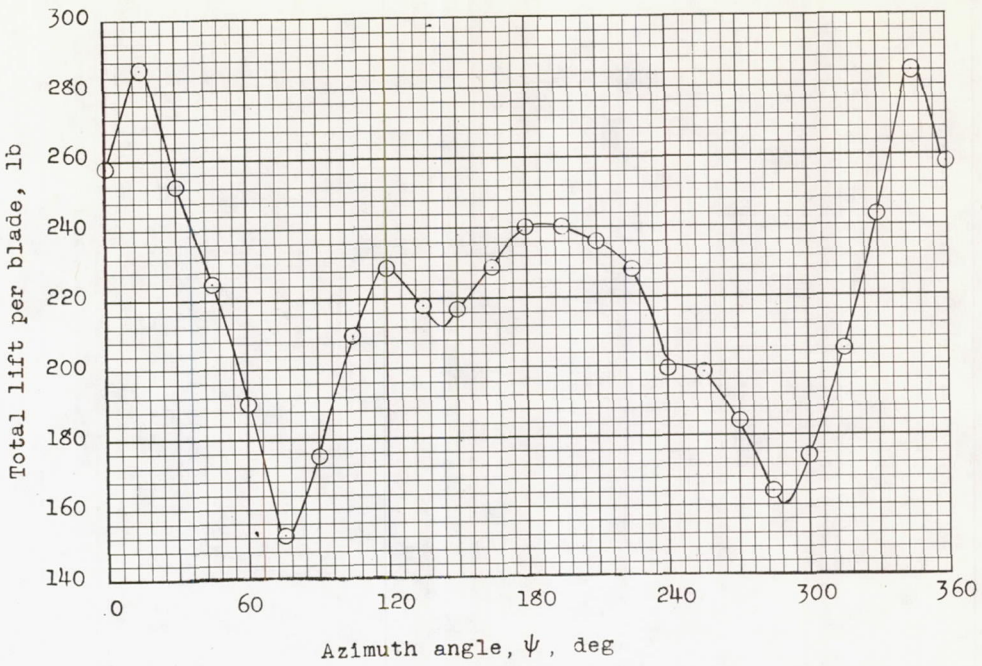

(c) $\mu = 0.15$.

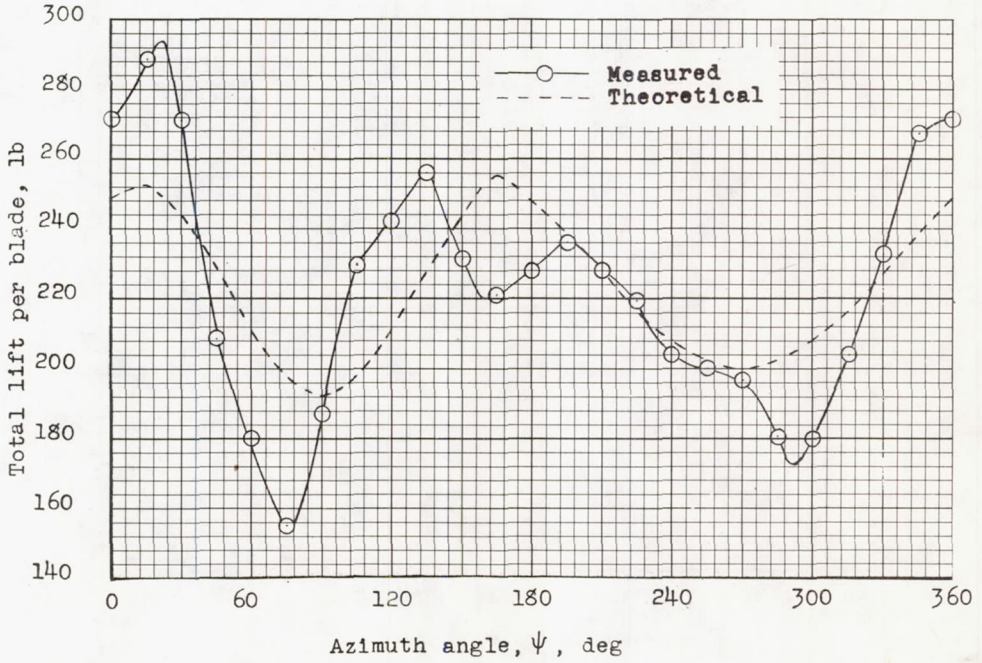

(d) $\mu = 0.20$.

Figure 12.- Continued.

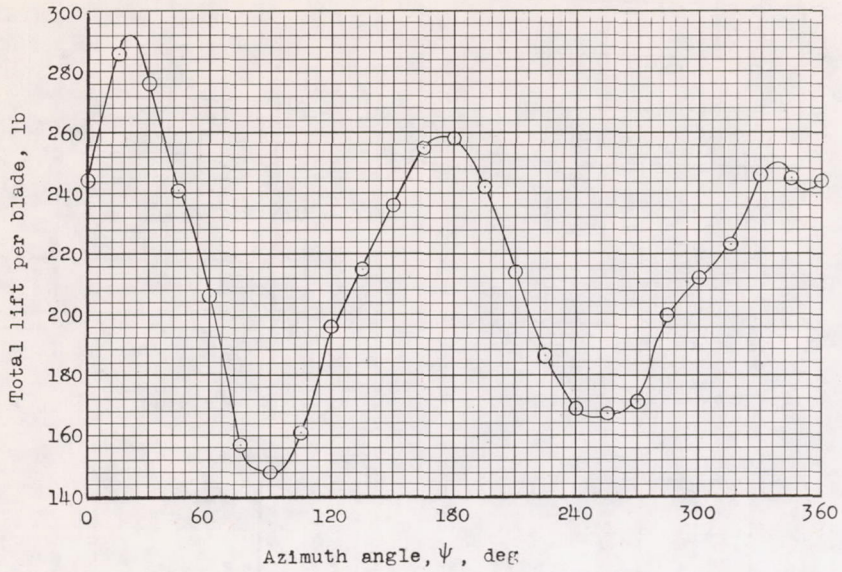

(e) $\mu = 0.24$.

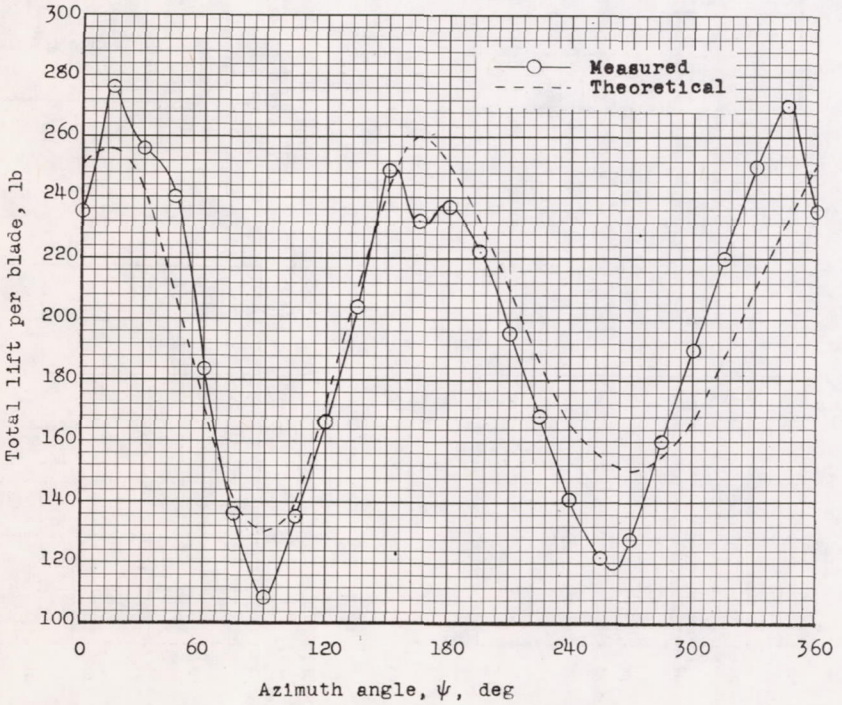

(f) $\mu = 0.29$.

Figure 12.- Concluded.

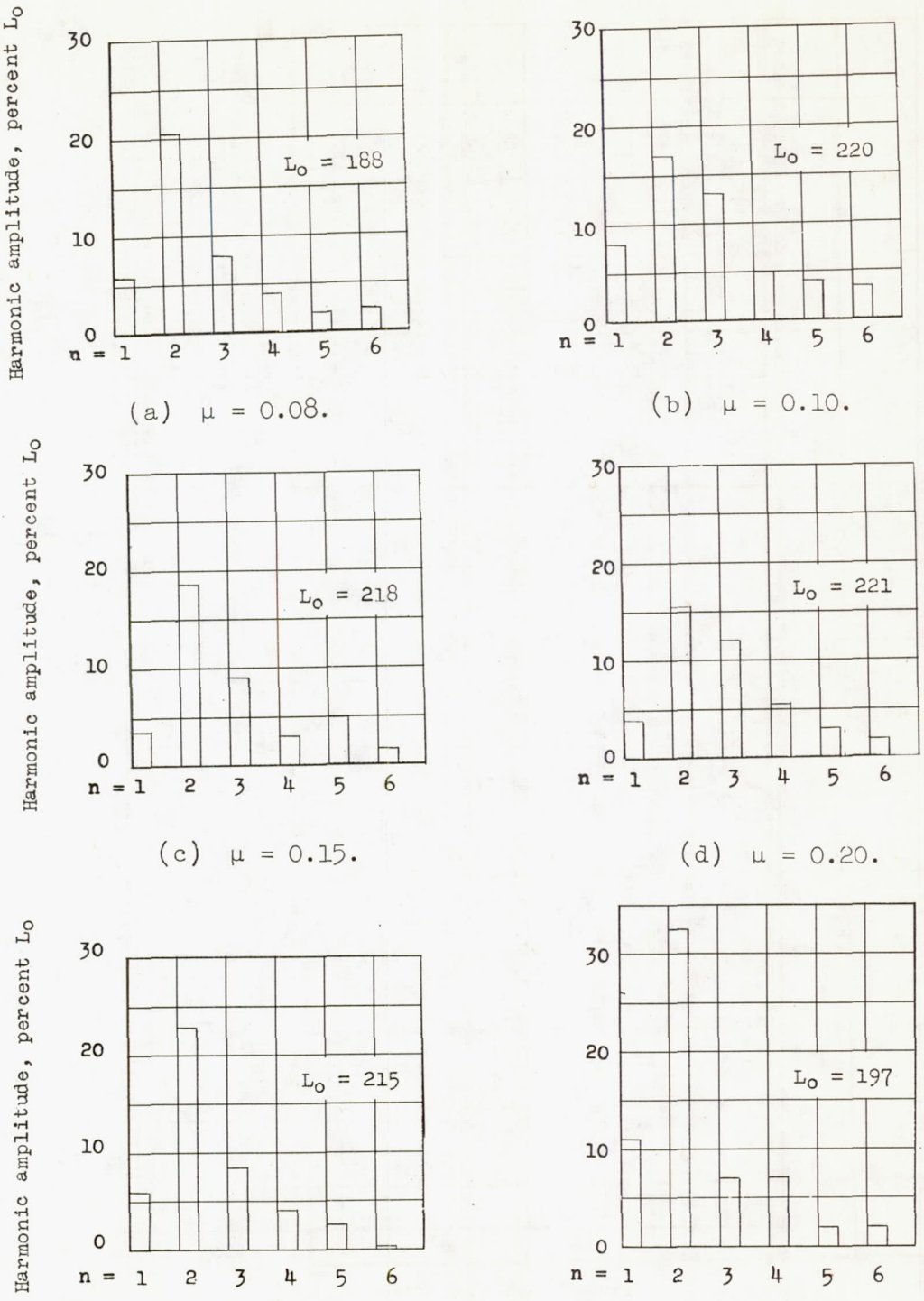

Figure 13.- Harmonic amplitude of total blade lift as percent of steady lift.

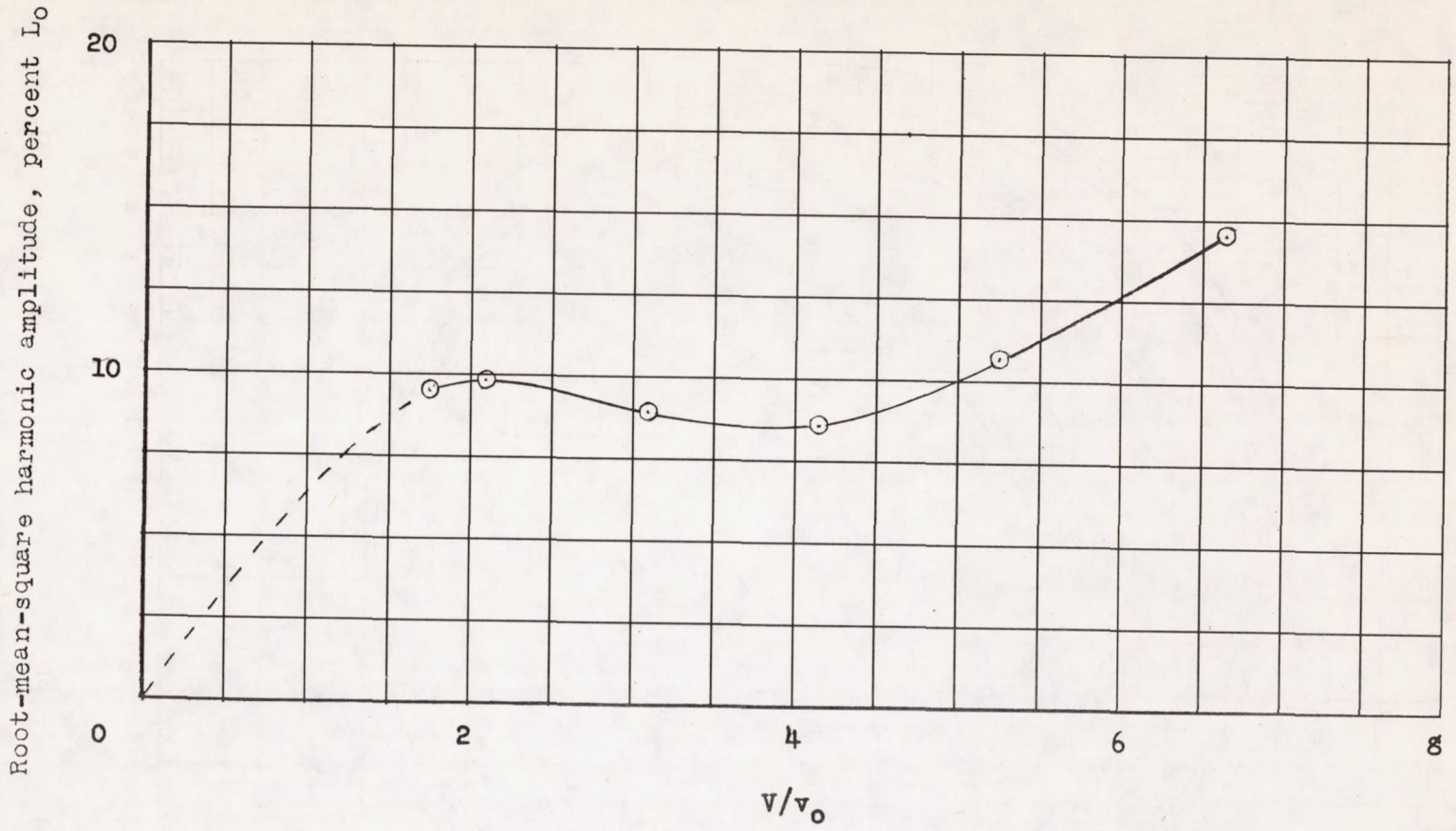

Figure 14.- Variation of root-mean-square harmonic amplitude of total blade lift, as percent of steady lift, with velocity ratio.

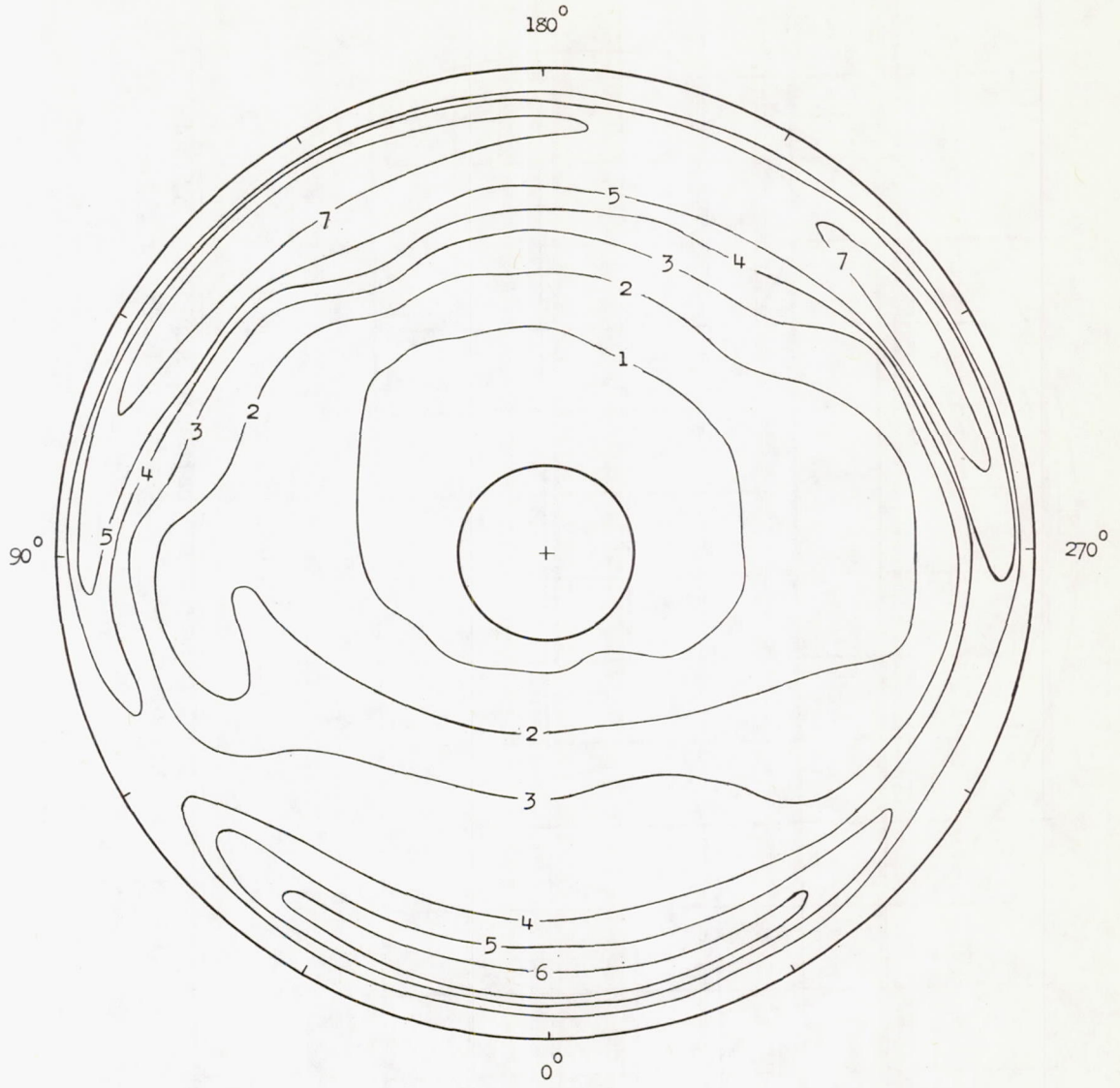

(a) $\mu = 0.08$; $\alpha = -1.1^{\circ}$; $C_{T_p} = 0.00367$.

Figure 15.- Contours of aerodynamic loading in pounds per inch.

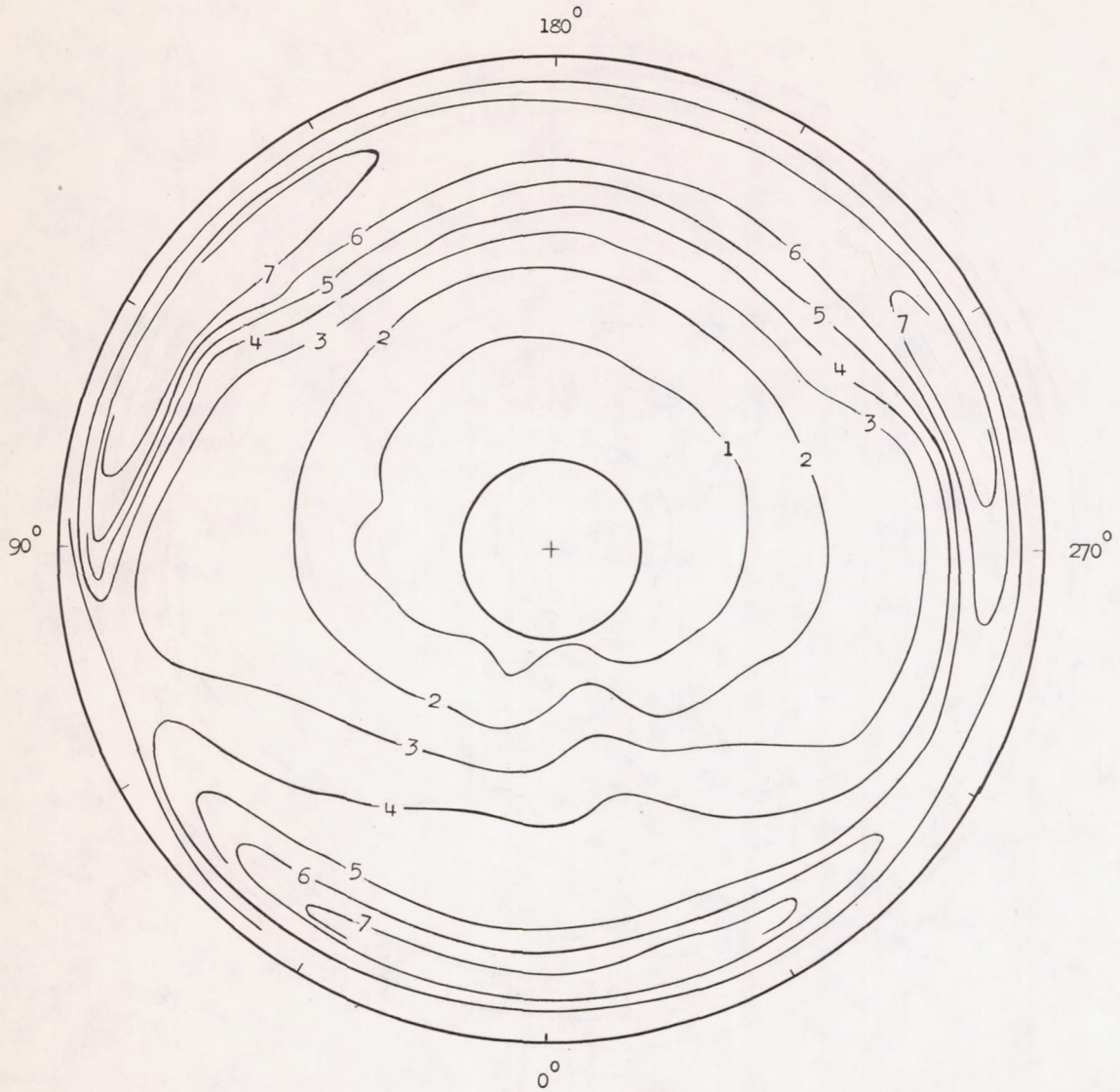

(b) $\mu = 0.10$; $\alpha = -1.9°$; $C_{T_p} = 0.00440$.

Figure 15.- Continued.

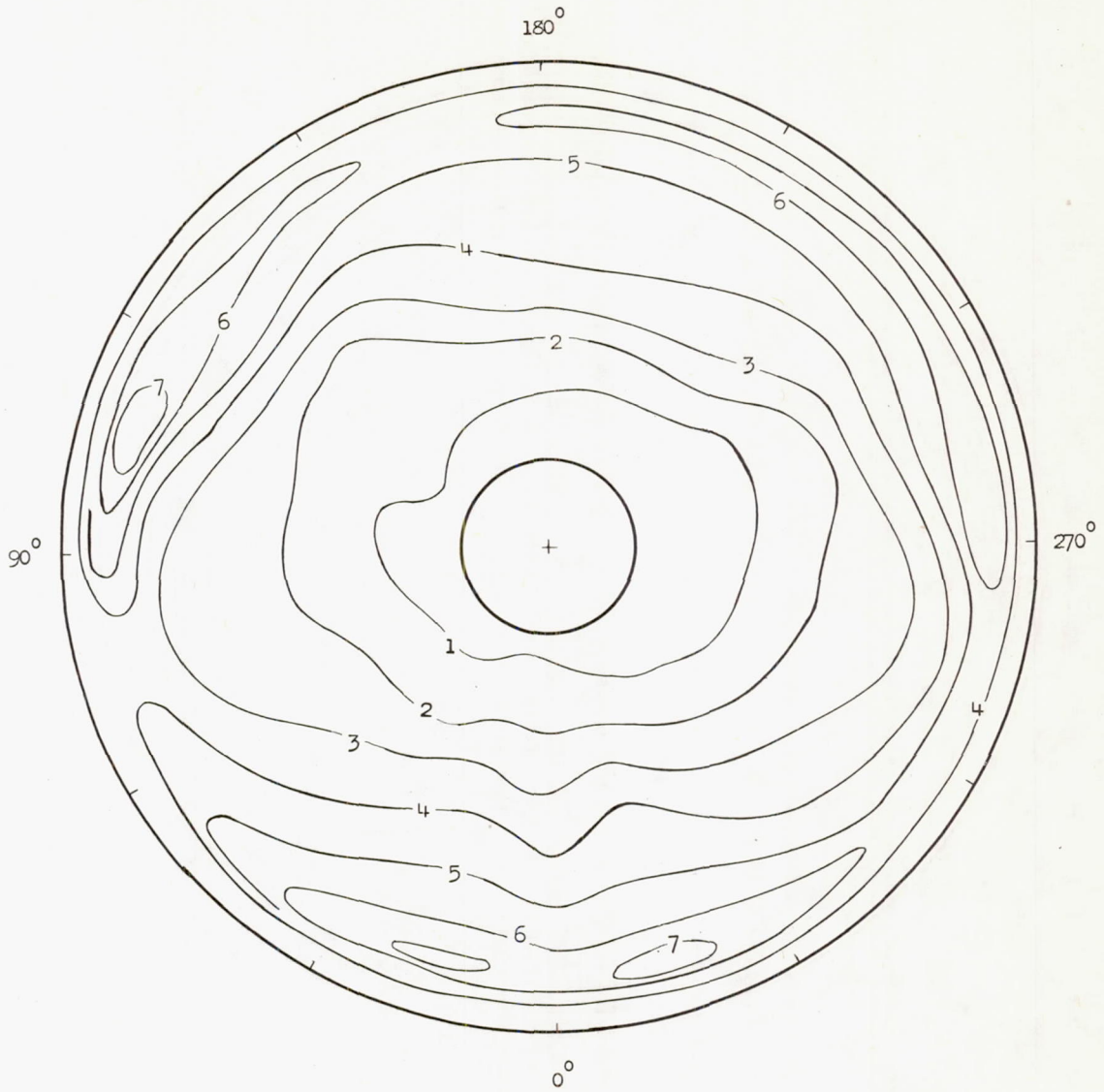

(c) $\mu = 0.15$; $\alpha = -4.0°$; $C_{T_p} = 0.00482$.

Figure 15.- Continued.

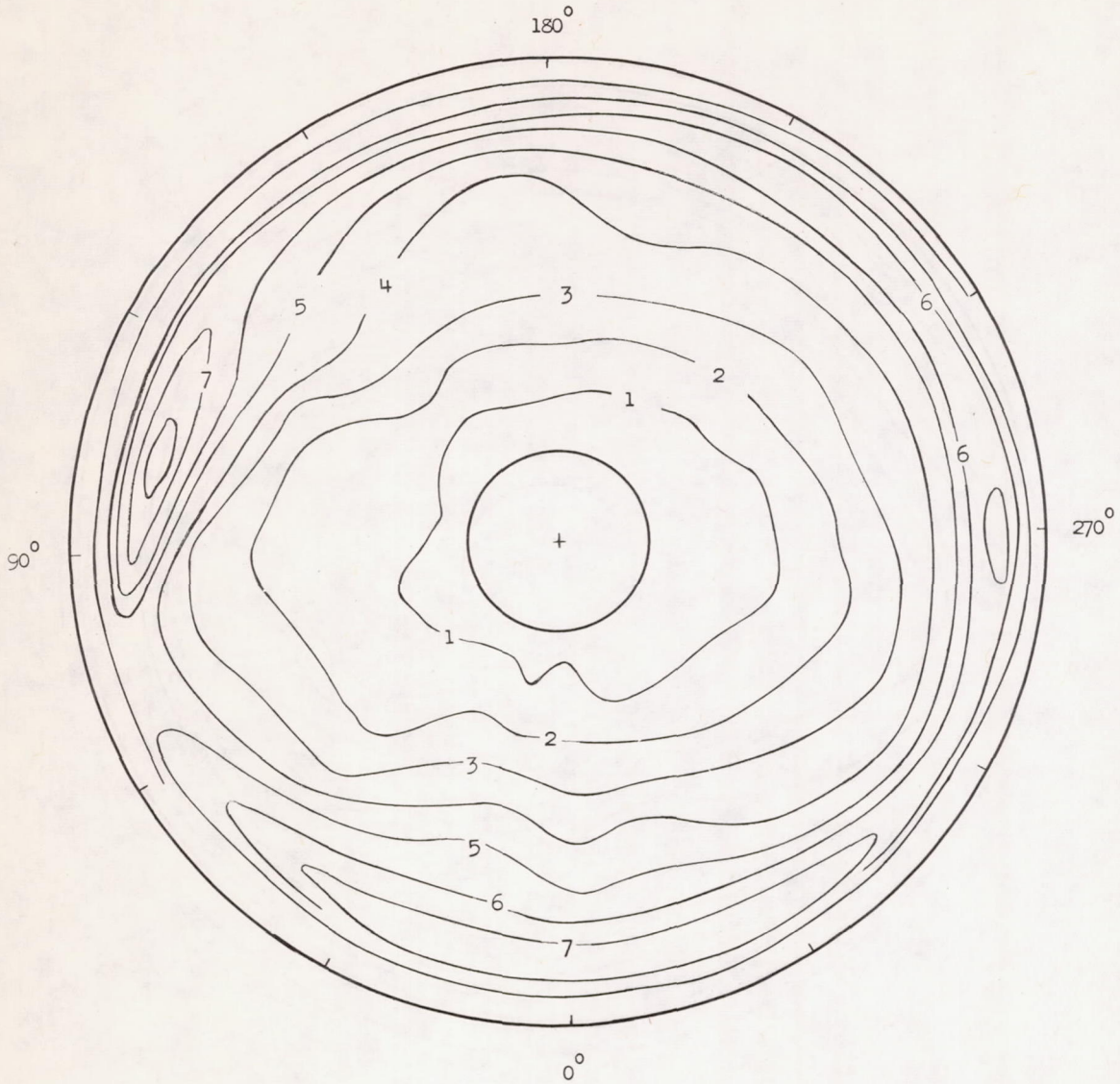

(d) $\mu = 0.20$; $\alpha = -6.8^{\circ}$; $C_{T_p} = 0.00460$. Shaded area denotes reversed-velocity region.

Figure 15.- Continued.

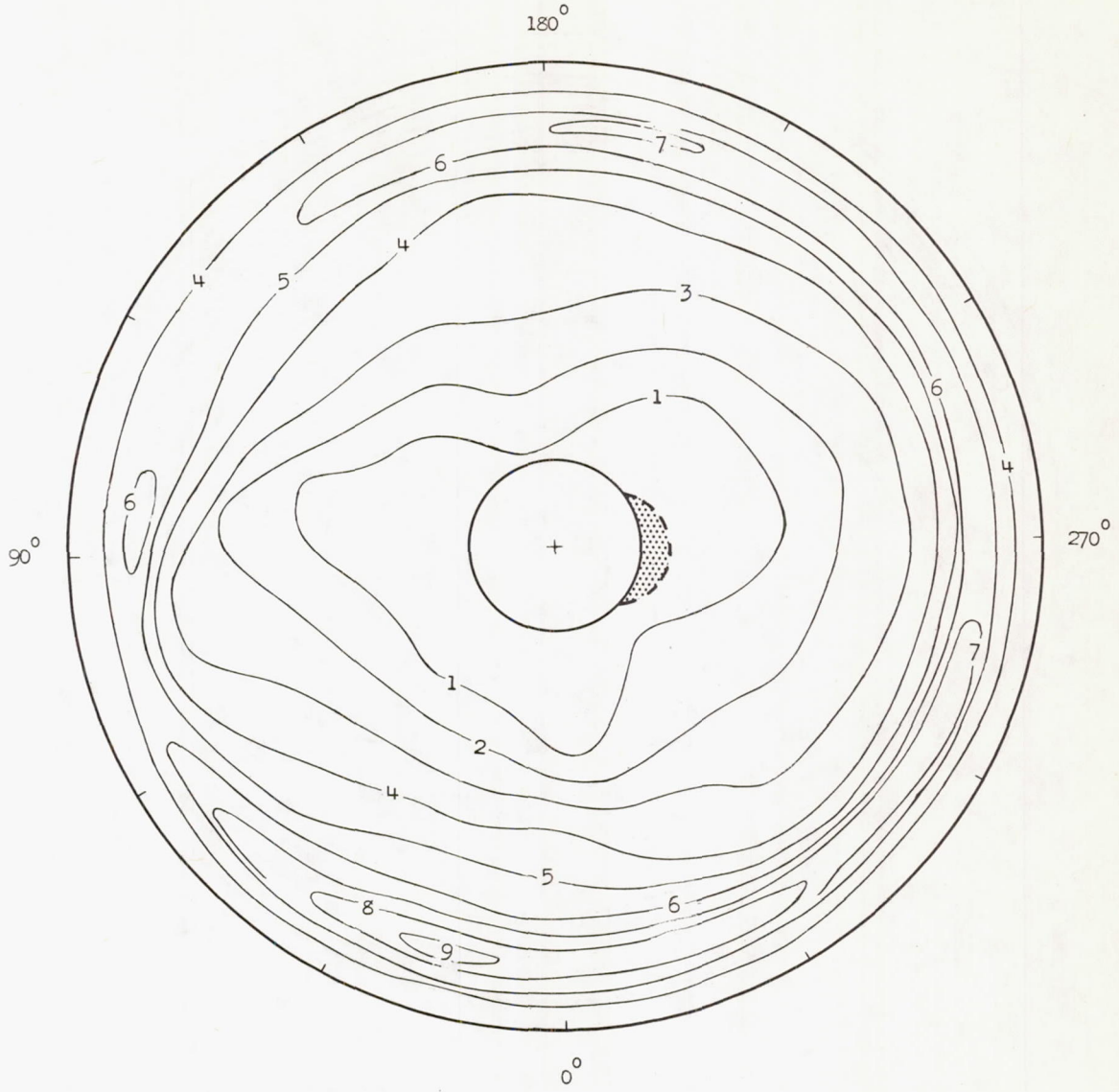

(e) $\mu = 0.24$; $\alpha = -9.8^{\circ}$; $C_{T_p} = 0.00436$. Shaded area denotes reversed-velocity region.

Figure 15.- Continued.

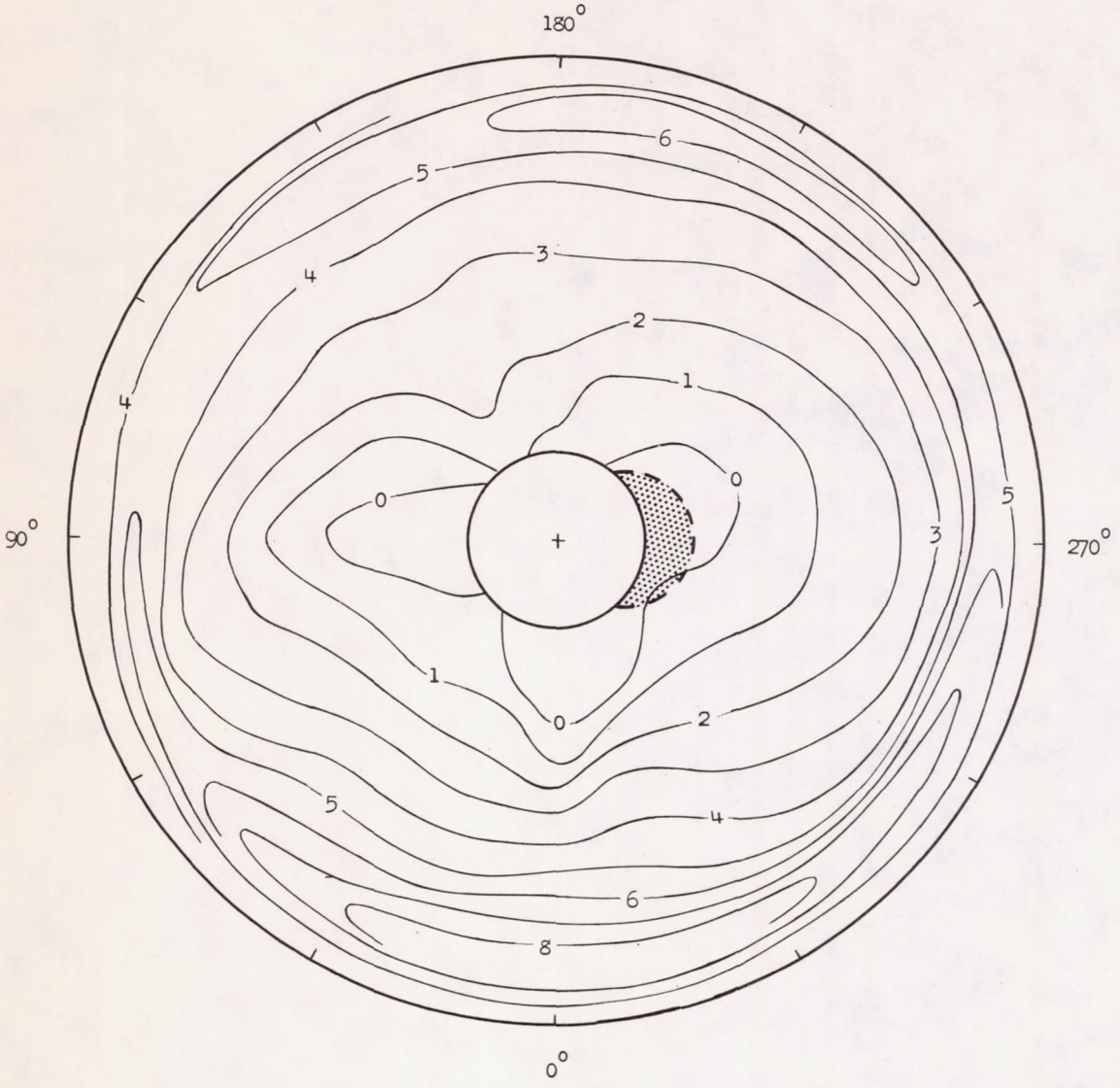

(f) $\mu = 0.29$; $\alpha = -11.7^{\circ}$; $C_{T_p} = 0.00394$. Shaded area denotes reversed-velocity region.

Figure 15.- Concluded.